ORIGINAL PAPER

Numerical Analysis of the 650,000 m² Åknes Rock Slope based on Measured Displacements and Geotechnical Data

Vidar Kveldsvik · Herbert H. Einstein ·
Bjørn Nilsen · Lars Harald Blikra

Abstract The unstable 650,000 m² Åknes rock slope (Western Norway) poses a hazard, as a sudden failure may cause a destructive tsunami in the fjord. In this study the slope was divided into blocks based on displacements measured at the slope surface. Discontinuous deformation analysis (DDA) showed that three or four blocks in the upper half may be considered as potential subareas that may fail catastrophically. The lower half may be divided into two or three blocks, but more limited data introduces more uncertainty into block definition. The Universal Distinct Element code (UDEC) was used for two-dimensional (2D) stability analyses. By varying fracture geometry, fracture friction, and groundwater conditions within reasonable limits based on site-specific data a number of possible models were compared. The conclusions show that models that were unstable to great depths were in closer agreement with shear strength parameters derived from an earlier study than models that were unstable to smaller depths. The length (depth) of the outcropping fracture, along which shear displacements are shown to occur, plays an important role. A (shallow) slide at 30 m, in which displacements have been documented by borehole measurements, will reduce the stability at greater depths. Increased groundwater pressure is demonstrated to be less critical for very deep slope instability. The results of the DDA and UDEC modelling will be useful for

V. Kveldsvik (✉)
Norwegian Geotechnical Institute/International Centre for Geohazards, Oslo, Norway
e-mail: Vidar.Kveldsvik@ngi.no

V. Kveldsvik · B. Nilsen · L. H. Blikra
Norwegian University of Science and Technology, Trondheim, Norway

H. H. Einstein
Department of Civil and Environmental Engineering, Massachusetts Institute of Technology, Cambridge, MA, USA

L. H. Blikra
Geological Survey of Norway, Trondheim, Norway

planning of future investigations, interpretation of the subsequent results, further development of the early warning system and in the tsunami modelling.

Keywords Landslides · Displacement analysis · Numerical modelling · DDA-Backward · UDEC

1 Introduction

Landslides due to massive rock slope failures represent a major geological hazard in many parts of the world and have been responsible for some of the most destructive natural disasters in recent history. Landslide volumes cover at least five orders of magnitude between 10^5 and 10^{10} m^3 (Evans et al. 2006). Secondary processes associated with massive rock slope failures include landslide-generated waves (tsunamis) and displaced water effects and those associated with landslide dams (e.g. Blikra et al. 2005, 2006; Fritz et al. 2001; Müller-Salzburg 1987; Govi et al. 2002). The unstable Åknes rock slope in Western Norway is an example of the hazard being posed by a possible landslide generated tsunami, and not by the possible landslide itself (Fig. 1).
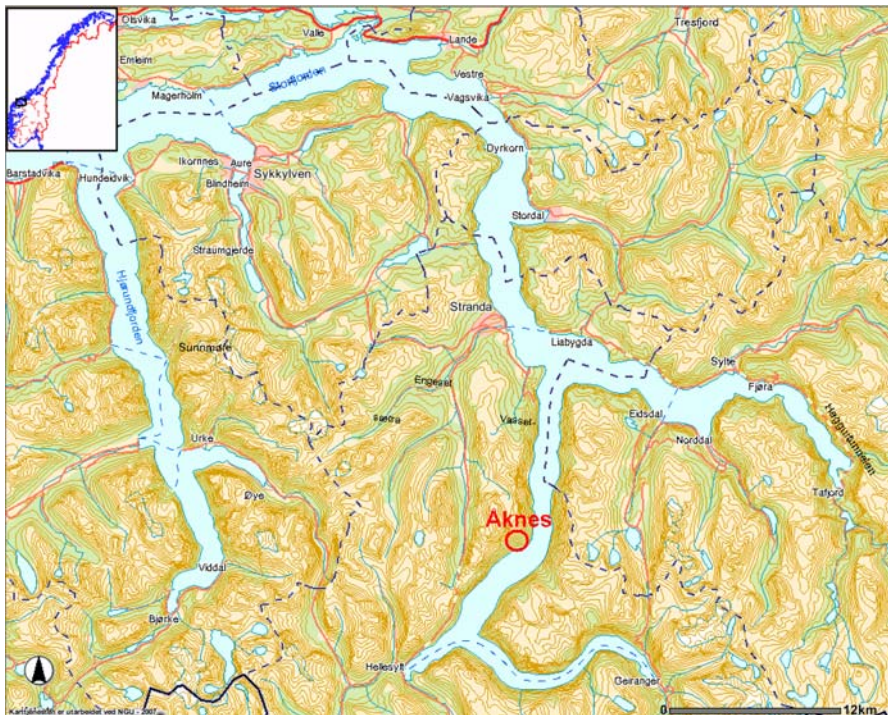
Fig. 1 Map of Storfjorden showing the location of the Åknes rock slope

Initial failure may be preceded by observable slope deformation manifested in growth and widening of tension cracks, increased rock fall activity and increasing disaggregation of the initial failure mass on the slope (Evans et al. 2006). Slope deformations and dislocations have close relationships with pre-collapse creep, i.e. long-term slow movements that take place under gravitational stresses smaller than the rock mass strength (Varga 2006). Ter-Stepanian (1966) identified different types of depth creep in rock slopes, including planar depth creep on long slopes with strata dipping parallel to the slope and rocks having different rheological characteristics. Slow displacements of the approximately slope-parallel active creep zone may be restrained by flattening of the sliding surface due to folding that acts as an obstacle (Varga 2006). Before a creeping slope fails catastrophically, it will undergo an acceleration phase, which can be used to predict time to failure (Voight 1989; Petley et al. 2002; Kilburn and Petley 2003; Crosta and Agliardi 2003; Fukuzono 1985).

In recognition of the controlling influence that jointing has on complex slope deformation, discrete element techniques are being used increasingly for numerical modelling. Two principal methods are in use: the distinct element (Hart 1993) and discontinuous deformation analyses (DDA) (Shi and Goodman 1989), of which the former is most commonly used in engineering practice (Stead et al. 2006). Some recent examples of discrete element analyses are those by Segalini and Giani (2004) who used the Universal Distinct Element code (UDEC) (Cundall 1980) to analyse the evolutionary mechanisms of a 30 million m³ rock slide (the Randa rock slide), Bhasin and Kaynia (2004) who used UDEC to estimate the potential failure volume of the rock mass of a 700 m high slope under static and dynamic forces and Sitar et al. (2005) who used DDA to analyse two typical examples of slope failure and demonstrated that accurate representation of the discontinuity geometry is essential for the identification of the kinematically correct failure modes. Sitar et al. (2005) also analysed the 200–300 million m³ Vaiont landslide and found that the location and number of discontinuities had a significant effect on the predicted stability and failure velocities of the landslide. Progressive failure of intact rock and fracture propagation, which may be an important failure mechanism in jointed rock slopes, have been modelled by the hybrid finite/discrete element code ELFEN (Eberhardt et al. 2004a, b; Stead et al. 2006).

An early warning system is being implemented at the Åknes rock slope. The most visible sign of instability is the upper tension crack, where widening of the gap and elongation towards the east have been recognised by the local population since the late 1950s/early 1960s. Depressions in the talus and open fractures in the upper half of the slope are also visible signs of instability. The instability is caused mainly by the unfavourable orientation of the foliation of the gneisses, which is subparallel to the slope surface (Braathen et al. 2004; Kveldsvik et al. 2006, 2007). Widening of the upper tension crack has been monitored since 1986 (Kveldsvik et al. 2006) and today movements on the slope surface and in boreholes are monitored by various techniques (Blikra 2008). Comprehensive investigations at the site are described by Ganerød et al. 2008. The main objectives of the study presented herein were to evaluate the probable division of the unstable area into subareas (subblocks) based on displacements measured on the slope surface and to evaluate the depth of instability based on data on fracture geometry, fracture friction and groundwater

conditions. The former analysis was undertaken using DDA and the latter using UDEC version 3.10. The results of this study will be useful for planning future investigations and interpretation of the subsequent results, for further development of the early warning system and in the tsunami modelling (rock slide volume estimates).

2 Methods

2.1 Displacement Analysis

The backward modelling mode of the discontinuous deformation analysis (DDA), hereafter referred to as DDA-Backward, was used for block analysis based on the measured displacements. DDA originated from a back-analysis algorithm for determining a best fit to a deformed configuration of a block system from measured displacements and deformations (Shi and Goodman 1985). It was later further developed to perform complete deformation analysis of a block system (Shi 1988). The early formulation used a simple representation of block motion and deformation, with six basic variables (three rigid-body motion and three constant-strain components) and is not suitable for irregularly shaped blocks. The major improvements come from full internal discretization of blocks by triangular or four-node finite element modelling (FEM) elements (Shyu 1993; Chang 1994), as also demonstrated by Jing (1998). These improvements make the DDA method more suitable for arbitrarily shaped deformable blocks. Numerous other extensions and improvements have been implemented over the years, with the bulk of the publications appearing in a series of ICADD conferences (Jing 2003). More than 100 DDA validation studies are summarised in MacLaughlin and Doolin (2006) and MacLaughlin and Berger (2003). Despite the numerous publications on DDA, application of DDA-Backward appears to be rare. Published studies include Shimizu et al. (1996) and Yeung and Blair (1999, 2000).

DDA-Backward uses displacements measured at individual points as input to compute the movement and deformation of whole block systems. The output data are the least-square best-fit block displacements and strains and the relative sliding and opening of interfaces between blocks, which together allow determination of global stability. These data can be used to judge whether failure has occurred for an entire block system. The backward analysis may be used to compute the Young's modulus and Poisson's ratio from displacement measurements. Backward analysis through an interpretation of measured displacements provides material constants, initial stresses of the rock mass and possible boundary conditions for further forward analysis (Shi 1988).

In this study DDA-Backward was used solely to determine possible subdivision of the unstable area into blocks. The main inputs for the analyses were assumed block boundaries for different models and the measured displacements. The outputs from each analysis were the computed average displacement error of all the measuring points in the whole model, the strains in each block and the opening of block boundaries. The displacement error for one single measuring point is the

difference between the displacement in the model after computation and the measured (input) displacement. The average displacement error was used primarily for the evaluation of the validity of models, i.e. the best model is the model with the lowest average displacement error. The strains were also considered, and in models with approximately equal average displacement errors, the model with the smallest strains was considered the best model. Generally, if useful field data exist on strains in some subareas of the area to be analysed, one would probably consider a model with computed strains comparable with the field data in these subareas to be better than another model, even though the latter shows smaller strains.

Developing the different models involved drawing block boundaries that seemed plausible with respect to the measured displacements and the geological model. The block boundaries based on the geological model (Ganerød et al. 2008) were the starting point for the modelling work (Figs. 2, 3). The numerical models presented in this paper may therefore be considered as a test of this geological model with respect to possible refinements/new data. Alternatively DDA-Backward could serve as the starting point of a geological study provided that displacement data exist, and field investigations could initially focus on verifying or rejecting the DDA-Backward-derived block boundaries.

DDA-Backward is illustrated by two simple examples of block slide geometries in Figs. 4 and 5. Figure 4 illustrates the importance of also evaluating the block strains, i.e. the model was unacceptable before the lower block was removed, showing that the upper block must move independently of the lower block. In other words, the surface on which the upper block moves must daylight at the boundary of the blocks (or somewhere below the points where displacements have been measured). Figure 5 illustrates that the minimization of displacement error may produce a deformed shape of the block that is forced to move, that the average displacement error dropped from 0.23 to 0 when the upper block was split in two parts and that the displacement pattern in the upper figure indicates that the block must be split in two parts to produce an acceptable model. This illustrates that the perhaps most important step of the analysis is to study the displacement patterns carefully and draw the block boundaries of relevant models accordingly, then the computations will determine the best model. A unique solution does not exist; one has to test different models and compare their average displacement errors and strains. It should be noted that the displacement error at each measuring point is shown as a line which points outside the circle (Fig. 5, middle) as in subsequent illustrations of DDA-Backward results.

The most important inputs for DDA-Backward are the block boundaries and displacements. One must also pay attention to other input parameters, and most important are the program steering parameters. The *maximum allowable displacement ratio* is the maximum allowable displacement per timestep divided by half the vertical dimension of the entire model. The recommended range is 0.0001–0.02, and 0.01 or lower was used in the computations presented here. Values equal to 0.02 and higher were tested on some models and worked poorly. If one uses low values, the specified total time (number of timesteps × time interval) may not be reached in the computations since the time interval in some timesteps may be made shorter than the specified value to satisfy the maximum allowable displacement ratio per
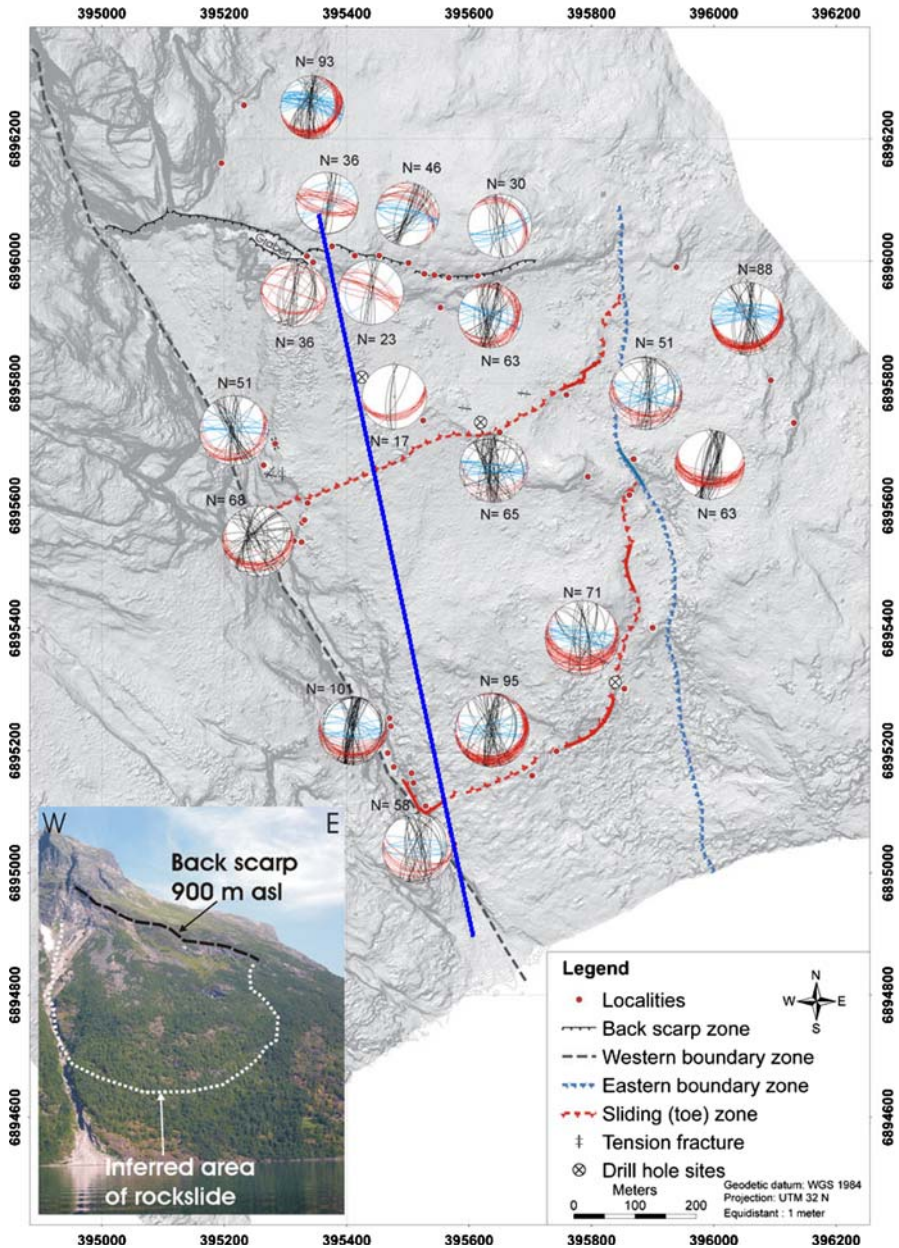
Fig. 2 Relief map of the Åknes rock slope with stereographic presentation of the fracture distribution (lower hemisphere, equal area). *Black* ∼N–S trending fractures. *Blue* ∼E–W trending fractures. *Red* fractures parallel to the foliation. *Blue solid line* profile for modelling of cross sections. Assumed area of unstable rock is marked in the inset (photo by M. H. Derron). Adapted from Ganerød et al. (2008)
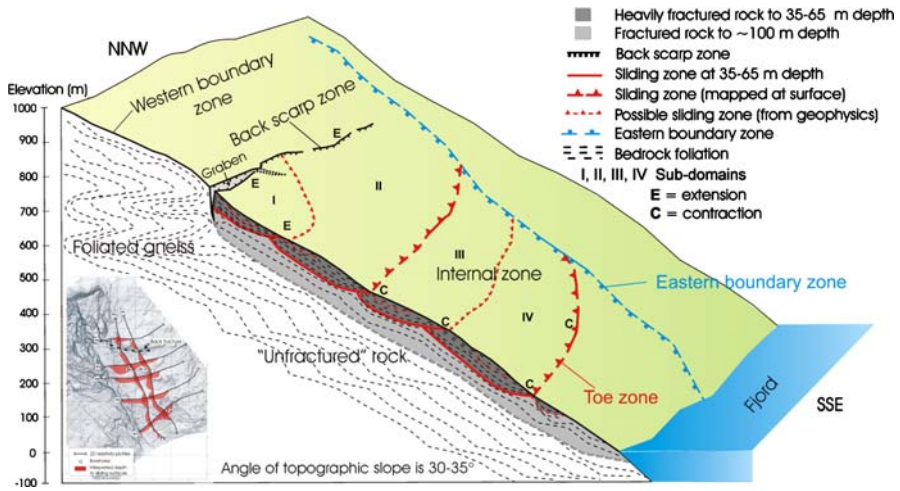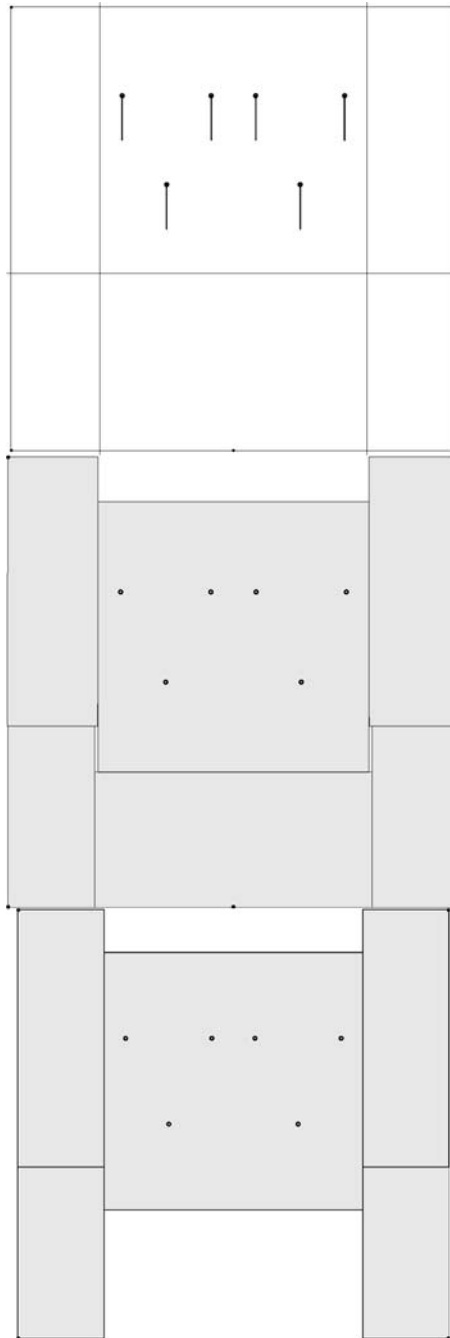
Fig. 3 Geological model of the Åknes rock slope. The inset (*lower left*) shows the thickness of unstable rock mass as interpreted from geophysical data. Adapted from Ganerød et al. (2008)

timestep. This leads to incorrect results, i.e. too high average displacement error. A very small time interval is acceptable as long as the specified total time is reached, however with some restrictions as described below.

The *time interval* must be large if full damping is applied, as the average displacement error will increase and the strains will decrease with decreasing time interval. Full damping means that the *dynamic coefficient* is set to zero, implying that the velocity is reset to zero at the start of each timestep. Using dynamic coefficient in the range 0.95–0.999, i.e. 95–99.9% of the final velocity of the previous time step is used as the initial velocity of the next time step, will reduce the dependency of the time interval to a negligible level. Any figure between 0.95 and 0.999 will normally be acceptable, but problems may arise if a high dynamic coefficient is combined with a very small time interval as this may cause unstable computations. The dynamic coefficient was set to 0.95 for all the computations in this study. The *stiffness of the contact spring* should normally be calculated by the program. However, for different visualisation and perhaps better understanding of a model it might be useful to experiment with soft contact springs, implying that overlaps between blocks may occur.

The physical parameters are less important in the geometric backward model. Some comments are nevertheless worth noting: *density* should be given a realistic value, although the computations may give reasonable results even with unrealistic densities, depending on the number of measuring points. Unrealistically small values of *Young's modulus* may cause poor performance of the computations. *Poisson's ratio* should be set to an assumed (or known) realistic value: Fig. 4 shows that the lower block expanded in the lateral direction due to the Poisson's effect. However, if the lower block were fixed at the corners at the bottom of the block, and not only in the centre line, the enforced zero displacements would prevent the

block from expanding laterally, although it would still shorten in the vertical direction. The Poisson's effect is overruled by the enforced (in this case zero) displacements.

Fig. 5 *Upper* Before computation; measured displacements of different magnitude. *Middle* Average displacement error = 0.23 and block strain occurs. *Lower* Zero average displacement error, and zero block deformation. For all figures: *dots* along the outer boundary are fixed points
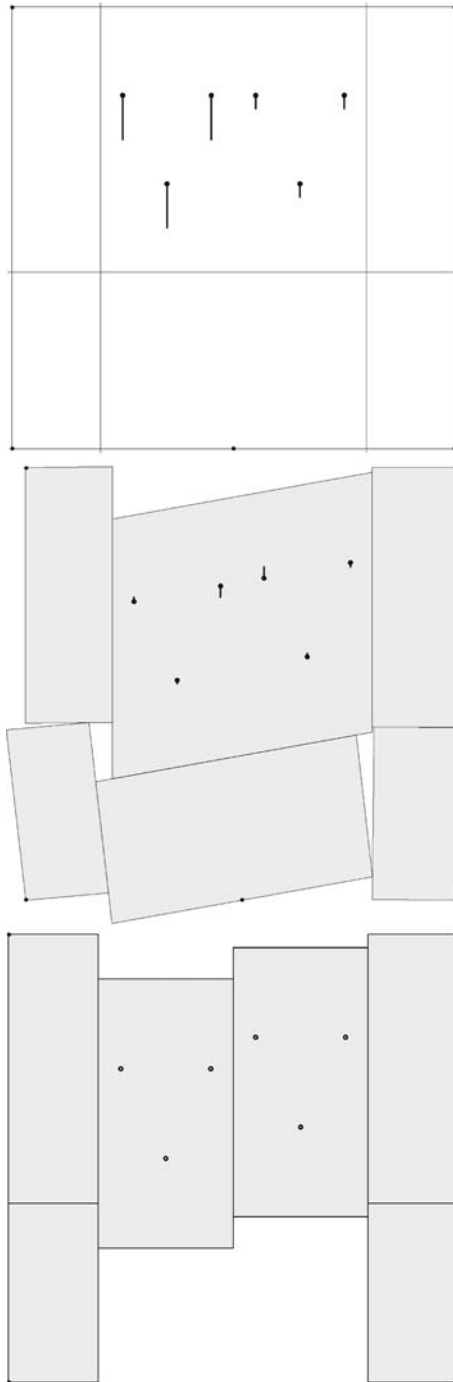
2.2 Stability Analysis

Modelling of vertical cross sections of the slope was performed using the Universal Distinct Element code (Cundall 1980, version 3.10.81). Most of the model geometry was constructed with the geometry module of DDA for Windows (MacLaughlin and Sitar 1995). The main objective of the modelling was to investigate the influence of fracture geometry (block boundaries), mechanical properties of fractures (friction) and groundwater pressure on the stability of the slope. Fractures parallel to the foliation (hereafter referred to as foliation fractures) and subvertical fractures with strike directions approximately E–W (hereafter referred to as E–W fractures) were included in the models (Fig. 2). Fractures with strike directions about N–S were not included since they are orientated subparallel to the cross sections and act as lateral releases. The friction angle of the different fractures was based on previous investigations of shear strength parameters as were the normal and shear stiffness of the fractures (Kveldsvik et al. 2007). The input parameters for calculation of deformable blocks properties are density (ρ), Young's modulus of the rock mass (E_m) and Poisson's ratio of the rock mass (v_m). These parameters were set to their mean values in all models: ρ = 2,738 kg/m^3, E_m = 22 GPa and v_m = 0.25 (Kveldsvik et al. 2007).

Each model assuming a fixed fracture geometry, groundwater table and deformable block properties was computed several times with varying fracture friction angles (see later) in order to determine the limiting friction angles for that specific model, i.e. the friction angles that were just large enough to result in equilibrium in the numerical model. The next step was to reduce the friction angles slightly to investigate the behaviour of a marginally unstable model. The logic here is that the (slow) movements that take place in the Åknes rock slope indicate that the rock slope is near the limit of equilibrium. As shown later the friction angles were in most models made dependent on the estimated effective normal stresses based on the Barton–Bandis shear strength criterion (Barton and Bandis 1990; Barton and Choubey 1977). The default equilibrium criterion of UDEC was used, i.e. a ratio limit of 10^{-5} of the average unbalanced force magnitude to the average applied force magnitude. In addition a large number of measuring points in the models were monitored with respect to displacements. Displacements do not increase with increasing number of time steps (cycling) when that particular part of the model is stable/in equilibrium.

3 Input Data for Numerical Modelling

3.1 Geological Model

Ganerød et al. (2008) proposed a geological model for the SSE facing Åknes rock slope (Figs. 2, 3). The model is based mainly on structural surface mapping, geophysical surveys (2D resistivity, seismic, ground-penetrating radar) and borehole logging (drill cores, geophysical logging). The interpretations of the geological data were supported by displacement data from the period 2004–2006. The limits of the

assumed unstable area in this study are the Back Scarp Zone, the Western Boundary Zone, the Toe Zone and the Eastern Boundary Zone. Further it was divided into four subdomains as shown in Fig. 3. The geophysical data indicate that the subdomains are bounded by four low-angle thrusts. It was concluded that the overall displacement pattern was an extension in the upper part (north) of the slope and contraction in the lower part (south) and that the folded foliation controls the development of the sliding surfaces. The maximum depth to the sliding surfaces was estimated to be 65–70 m based on geophysical surveys and borehole logging. In an earlier study Kveldsvik et al. (2006) estimated the movements in the slope to be restricted to depths of about 60 m based on core logging of four boreholes.

The Back Scarp Zone is about 800 m long. The elevation is 900 m above sea level (m.a.s.l.) in the western part and 700 m.a.s.l. in the eastern part. The western approximately 200 m consist of a cliff face and just east of this cliff face a 20–30 m deep and 10–25 m wide graben exists. Further to the east the Back Scarp Zone is exposed as an open fracture of typical width 1 m. The maximum depth of the open fracture is estimated to be about 60 m in the western part. The Western Boundary Zone is a NNW–SSE oriented strike slip fault which is exposed as a 15–25 m deep crevasse. The Eastern Boundary Zone is a pre-existing fault with dip 35–45° to the west. This structure is not well defined in the topography. The Toe Zone at about 180 m.a.s.l. is a sliding surface parallel with the foliation. The strike direction of the Toe Zone is subparallel to the strike of the slope and it daylights because the dip is more gentle than the dip of the slope, which is about 35° measured between the Back Scarp Zone and the fjord. Gouge exists in the Toe Zone in the form of discontinuous layers. The total area of the assumed unstable rock mass inside the boundaries described above is about 650,000 m². The volume of the unstable rock mass was estimated to 35–40 million m³ by Derron et al. (2005).

The assumed unstable rock mass consists of gneisses of the following main types: biotitic, granitic and dioritic gneiss. Biotite schists exist in layers of maximum thickness of 20 cm. Three distinct fracture sets were identified by Ganerød et al. (2008): fractures parallel to the foliation and subvertical fractures with strike directions approximately N–S and E–W, respectively (Fig. 2).

3.2 Displacements

#### 3.2.1 Displacements on the Slope Surface

Slope displacement has been recorded over a total of 43 years. Displacement data from the periods 1961–1983 (photogrammetric), 1983–2004 (photogrammetric) and 2004–2006 [global position system (GPS), total station and rod extensometers] were used to evaluate possible/plausible divisions into blocks by computation using DDA-Backward. The horizontal components of the measured displacement rates are shown in Figs. 6, 7 and 8. Displacement rates are shown as the measured total displacement during the relevant period divided by the number of years. Aerial photographs from 1961 and 1983, and orthophotos from 2004 were used for the photogrammetry.
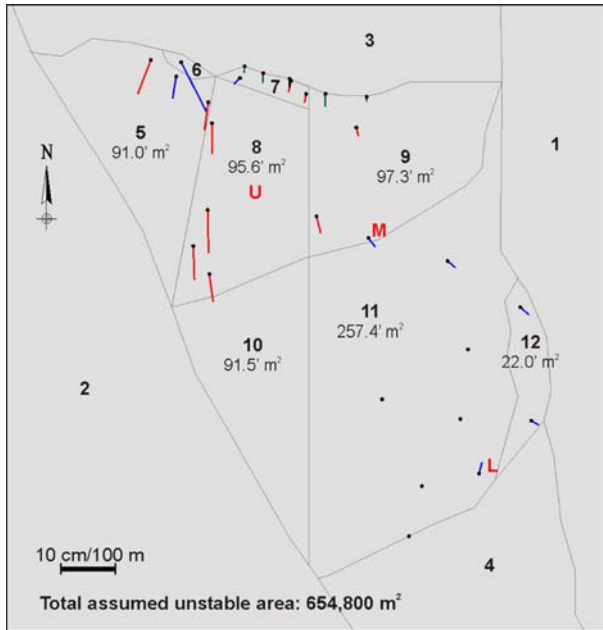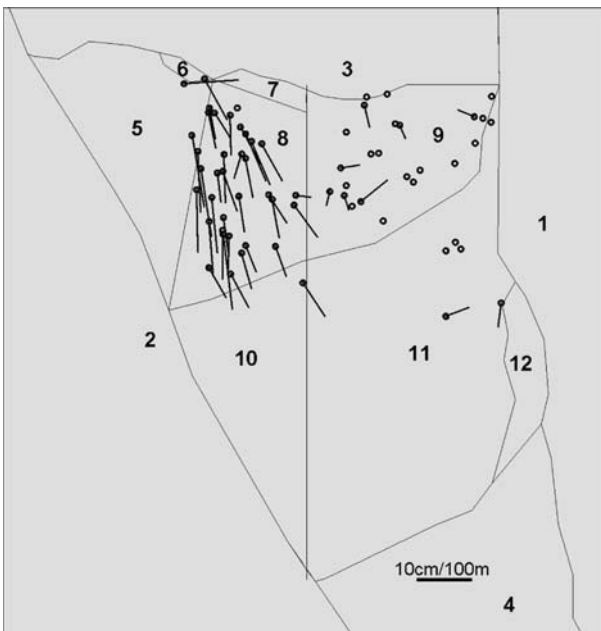
Fig. 6 Initial block model and annual average slope displacements 2004–2006. *Red* Total station, *blue* GPS, *green* extensometer. *Scale* cm for displacements, m for block model: 12 blocks. The *red letters* show the locations of the boreholes (upper, middle, lower). The whole model measures 1,100 m × 1,140 m

As mentioned above the 2004–2006 displacement data set includes measurements by rod extensometers (Fig. 6). The five rod extensometers, fixed in solid rock at both sides of the upper crack and with direction equal to or very close to N180° and inclinations from 26° to 50°, do not necessarily measure the maximum displacement over the upper crack, as discussed by Kveldsvik et al. (2006) and Ganerød et al. (2008). The calculated horizontal component of the measured displacement rates was used directly in this study. Other measuring points near the upper crack indicate that the extensometers measure most of the displacement over the upper crack. The whole data set is discussed in more detail by Ganerød et al. (2008); here the points with no displacement in block 11 are commented upon: some of the points with displacement equal to zero may indicate displacements, but their magnitudes are not significant compared to the accuracy of the method. The area with zero displacement in the horizontal plane may therefore be interpreted as insignificant or negligible movement. There may also be small upwards movements in block 11. However, it is too early to draw any conclusions about this based on the ongoing measurements.

The photogrammetric method is explained by Kveldsvik et al. (2006). The accuracy of the method is estimated to be 0.5 m, and only points that displaced more than 0.5 m from 1961–1983 and from 1983–2004, respectively, are shown with vectors in Figs. 7 and 8. In addition measuring points that displaced less than 0.5 m are shown as points without vectors. For both periods it is evident that block 9, especially
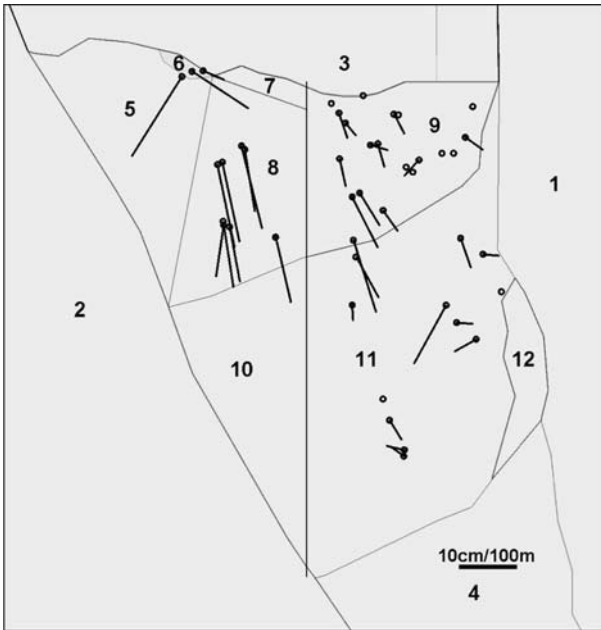
Fig. 7 Initial block model and annual average slope displacements derived from photogrammetry 1961–1983. *Scale* cm for displacements, m for block model

Fig. 8 Initial block model and annual average slope displacements derived from photogrammetry 1983–2004. *Scale* cm for displacements, m for block model

the eastern part, moved little. Few measuring points exist in the lower part of the slope, and no measuring points exist in the lower, western part (block 10). This reflects mainly that the slope was (and still is) more vegetated here and therefore it was difficult to find points that could be used (Eiken 2007). Block 10 was not measured from 2004 to 2006 either (Fig. 6) and therefore the current displacement of block 10 is not known.

The upper western part of the instability has moved considerably more than the rest of the slope. The calculated average value for vectors inside block 8 are: 12.6 cm/year for 1961–1983 (8 points), 7.7 cm/year for 1983–2004 (35 points) and 6.8 cm/year for 2004–2006 (4 points). Systematic errors in the photogrammetry could possibly be a reason for part of the difference, and the two data sets were controlled with respect to the magnitude of the measurements internal and external block 8. The external area also includes areas outside the area shown in Figs. 6, 7 and 8. The ratios between the average displacement rate values for the 1961–1983 and 1983–2004 measurements are 1.62 for points internal to block 8 and 1.27 for points external to block 8. Based on the logic that a systematic error would have shown up as the two ratios being approximately equal, it is concluded that block 8 moved relatively more than the rest of the slope in the period 1961–1983 and that it moved more in earlier time periods than it has done in later periods.

The 2004–2006 data set shows a direct southward movement direction for block 8, whereas the photogrammetry indicates a more SSE direction (N171° as the average for 1961–1983 and N164° as the average for 1983–2004).

3.2.2 Displacements in Boreholes

In total, seven boreholes have been drilled: two at the upper drilling site, three at the middle site and two at the lower site. Relative displacements in vertical boreholes have been measured in one of the upper boreholes since 14 September 2006 and in one of the middle boreholes (Figs. 2, 6) since 24 November 2006 by deflectometers, i.e. the differential monitoring of stability (DMS) system. DMS measurements thus started after the last date of the surface measurements reported above. The monitoring depth intervals are 32–82 m in the upper borehole and 16.5–66.5 m in the middle borehole.

The following preliminary conclusion based on measurements up to 31 July 2007 is that there was probably a relative displacement in the upper borehole at 51–52 m, corresponding to a maximum of 1 cm/year. This is much less than at the surface in the same area, where 6.8–12.6 cm/year has been measured (Figs. 6, 7 and 8). The results from the upper borehole were difficult to interpret, but by including the results of the core logging (Fig. 9) and the video inspection of the borehole (overbreak, loose rock fragments from 51 to 52 m) it seems very likely that some displacements actually occurred between 51 and 52 m. The small magnitudes of the borehole displacements compared with the surface movements clearly indicate that movements take place above 32 m and/or below 82 m. For the middle borehole it is clear from the DMS measurements that displacements occured at a depth of about 34 m, and that the magnitude corresponds to approximately 1 cm/year. Displacements at
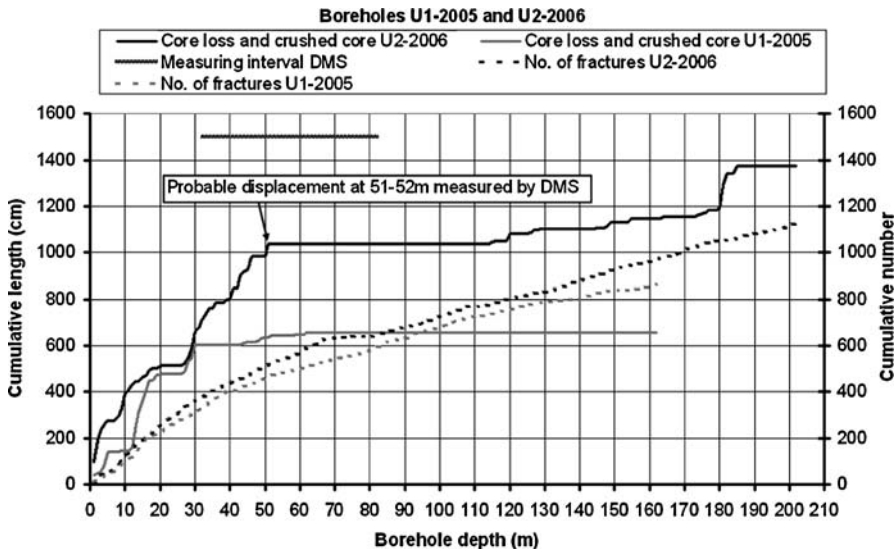
Fig. 9 Upper boreholes U1 and U2. Cumulative length of core loss/crushed core and cumulative number of fractures. Measuring interval DMS and location of measured displacement in U2
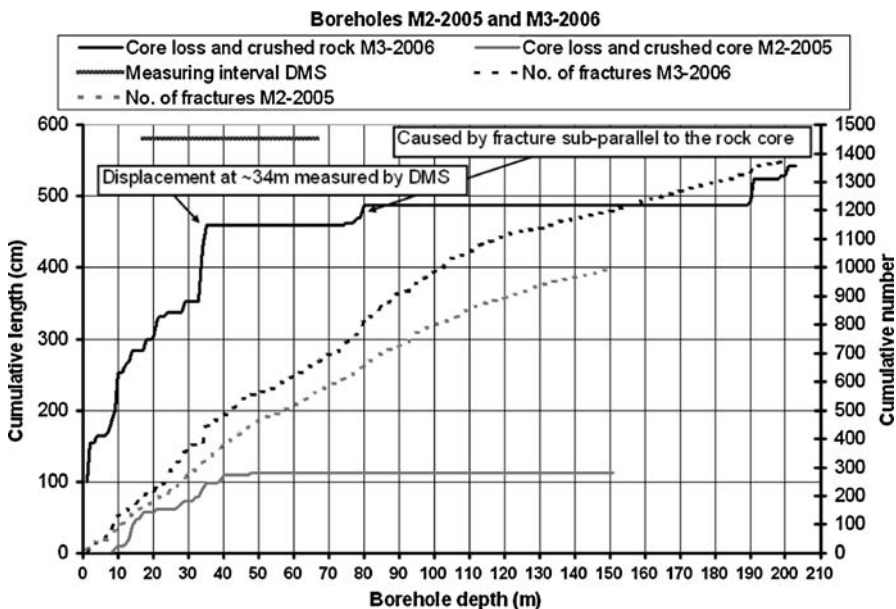

Fig. 10 Middle boreholes M2 and M3. Cumulative length of core loss/crushed core and cumulative number of fractures. Measuring interval DMS and location of measured displacement in M3

this depth also seem to agree with observations from the core logging (Fig. 10) and the video inspection of the borehole (overbreak/cavity, visible crushed rock, loose rock fragments, visible deviation in borehole direction). The displacement

magnitude measured at the surface a few metres away from the borehole and in block 9 generally in the period 2004–2006 is approximately 2 cm/year (Fig. 6).

3.3 Fracture Geometry

The orientations of the foliation fractures along and north of the Back Scarp Zone differ from the rest of the localities in that they are not orientated subparallel to the slope (Figs. 2, 11 and 12). Foliation fractures from the localities below the Back Scarp Zone were selected as the basic data set for the cross section models. Orientations of fractures nonparallel with the foliation are highly scattered (Fig. 13). The approximately N–S orientated fractures are most abundant. They were not included in the cross-section models as they are orientated subparallel to the cross sections and act as lateral releases. The less abundant E–W fractures were included in the cross-section models as vertical fractures. Apparent dip angles of foliation fractures in the profile used for numerical modelling (Fig. 2) are shown in Fig. 14. The apparent dip angles shown in Fig. 14 come from foliation fractures that differed up to ±20° in dip direction from the direction of the profile shown in Fig. 2.

The frequency of foliation fractures varies from 5 to 17 fractures per metre in the different zones of the unstable area according to Ganerød et al. (2008). The ratios of foliation fracture frequencies and nonfoliation fracture frequencies vary from 2.1 to 4.3. Figure 13 shows that only a fraction of the nonfoliation fractures are orientated approximately E–W. The approximate ratio of the fracture frequencies (foliation fractures compared to E–W fractures) is difficult to estimate with confidence. The
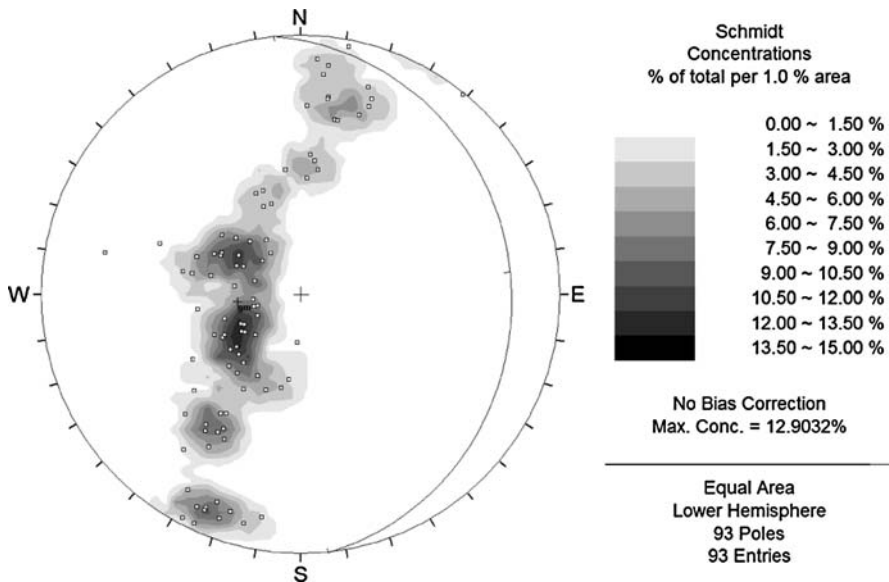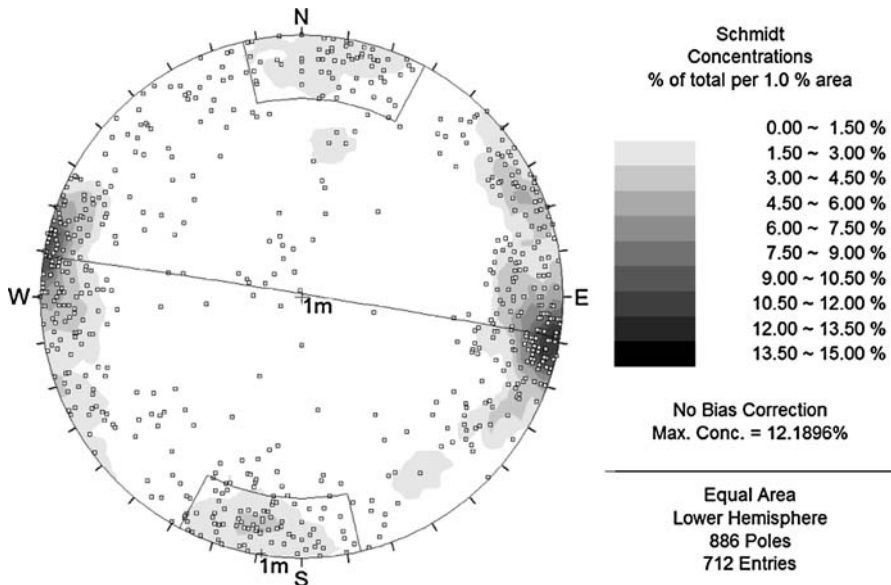

Fig. 11 Foliation fractures along the Back Scarp Zone. The global mean plane is orientated N354°/20°
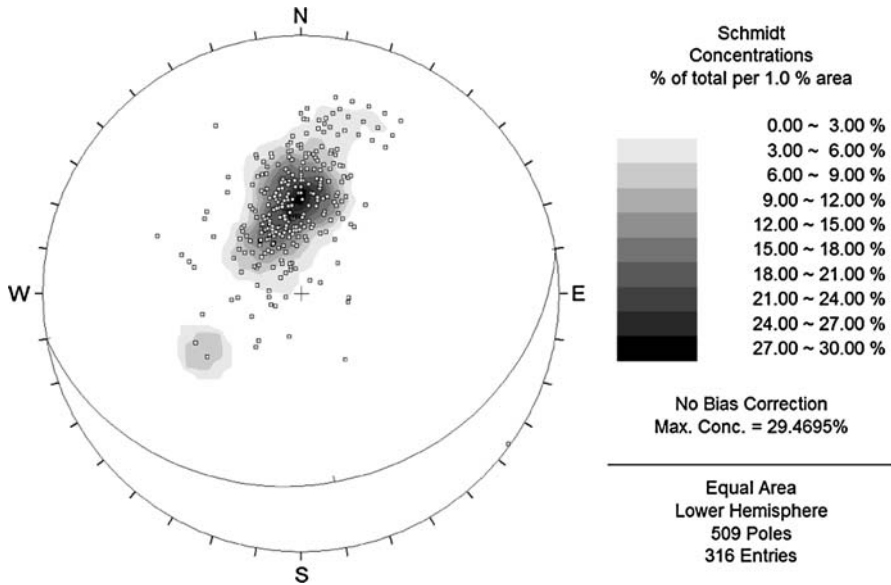
Fig. 12 Foliation fractures below the Back Scarp Zone. The global mean plane is orientated N080°/27°. The mean dip angle is 32°

Fig. 13 Fractures nonparallel with the foliation from all localities. The approximate E–W orientated fractures are indicated

spacing of E–W fractures was set to nine times the vertical spacing of the foliation fractures in most models. The vertical spacing of the foliation fractures, i.e. the possible sliding planes in the models, was set to 10 m, resulting in a spacing of 90 m
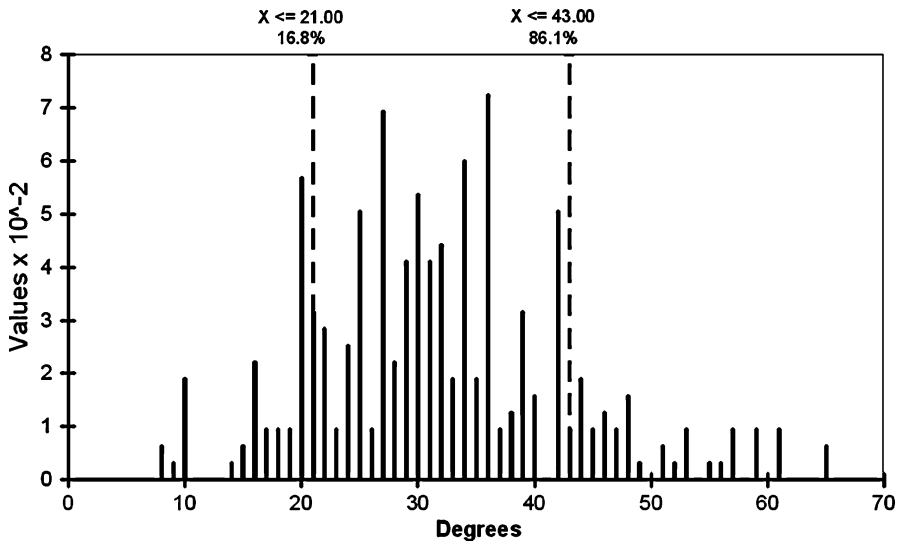
Fig. 14 Histogram of apparent dip of foliation fractures in the profile for numerical modelling. The interval inside the *broken lines* is the mean value (μ) $\pm$ standard deviation (σ): 31.8° $\pm$ 10.7°

for the E–W fractures in most of the models. The folding of the foliation that results in the assumed possible sliding daylighting in the slope surface (Fig. 3) were modelled as planar fractures and the inclinations of these fractures were varied.

3.4 Friction Angle of Fractures

Input parameters for the Barton–Bandis shear strength criterion (Barton and Bandis 1990, Barton and Choubey 1977) were derived for the Åknes rock slope by Kveldsvik et al. (2007). They showed that the joint roughness coefficient (JRC) had the greatest effect on the computed stability of a rock slide with a maximum height of about 28 m and a volume of about 100,000 m^3. The slide occurred on the western flank in 1960 or 1961 (Fig. 2, the slide scar of the intersection of the Western Boundary Zone and the middle slide zone). Sensitivity analyses using a deterministic limit equilibrium analysis assuming dry conditions and rock-to-rock contact along the failure surface gave a safety factor of 1.20 when all input parameters were assigned mean values. When a JRC of 6.0 was assumed with the other parameters assigned mean values, a safety factor of 1.0 was obtained. The mean JRC value was 7.8 and 41% of the JRC values measured on a 1 m scale were equal to or less than 6. The friction angles of the foliation fractures were in most models made dependent on the estimated effective normal stress in order to incorporate the nonlinearity of the Barton–Bandis shear strength criterion. A constant friction angle for the foliation fractures was also tested in some models to investigate the effect on the stability. The varying friction angle was calculated by deriving the Coulomb shear strength parameters from the Barton–Bandis shear

strength model (Barton and Bandis 1990; Barton and Choubey 1977); i.e. by calculating the instantaneous friction angle, φ_i from:

$$\tau = c_i + \sigma'_n \times \tan \varphi_i = \sigma'_n \times \tan \left[JRC \times \log_{10} \left(\frac{JCS}{\sigma'_n} \right) + \varphi_r \right], \qquad (1)$$

where τ is the peak shear strength, c_i is the instantaneous cohesion, σ'_n is the effective normal stress; φ_i is the instantaneous friction angle, JRC is the joint roughness coefficient, JCS is the joint wall compressive strength, and φ_r is the residual friction angle.

The residual friction angle was estimated (Barton and Choubey 1977) using

$$\varphi_r = \varphi_b - 20 + \left(20 \times \frac{r}{R} \right), \qquad (2)$$

where φ_b is the basic friction angle derived from laboratory tilt testing on sawn core pieces, r is the Schmidt hammer rebound obtained in situ on fracture surfaces, and R is the Schmidt hammer rebound obtained in situ on intact rock surfaces.

The effective normal stress was calculated using

$$\sigma'_n = \gamma_r \times d \times \cos^2 \alpha - (\gamma_w \times z_w), \qquad (3)$$

where γ_r is the unit weight of rock, γ_w is the unit weight of water, d is the vertical distance between the slope surface and the fracture, z_w is the vertical distance between the groundwater table and the fracture, and α is the inclination of the fracture.

Assuming that the instantaneous cohesion equals zero and combining Eqs. 1 and 2 gives for the active (secant) friction angle, φ_a:

$$\varphi_a = \left[JRC \times \log_{10} \left(\frac{JCS}{\gamma_r \times d \times \cos^2 \alpha - (\gamma_w \times z_w)} \right) + \varphi_r \right]. \qquad (4)$$

Substituting the mean values determined by Kveldsvik et al. (2007) of JCS in kN/m², γ_r in kN/m³ and φ_r in degrees in Eq. 4 gives for the foliation fractures:

$$\varphi_a = \left[JRC \times \log_{10} \left(\frac{133000}{26.86 \times d \times \cos^2 \alpha - (9.81 \times z_w)} \right) + 24.8 \right]. \qquad (5)$$

Application of Eq. 5 is illustrated in Fig. 15. Friction angles in this article are henceforth referred to by the corresponding JRC unless a constant friction angle has been used in the model in question. The friction angle of the E–W fractures was set to 49.5° unless stated otherwise. This friction angle corresponds to the average JRC, JCS, etc. of fractures nonparallel to the foliation (Kveldsvik et al. 2007) at an effective normal stress of 0.26 MPa.

3.5 Stiffness of Fractures

The method for estimating the normal and shear stiffness of fractures is explained in Kveldsvik et al. (2007). All input parameters were set at their mean values and the normal and shear stiffness were computed for different normal stresses (see above)
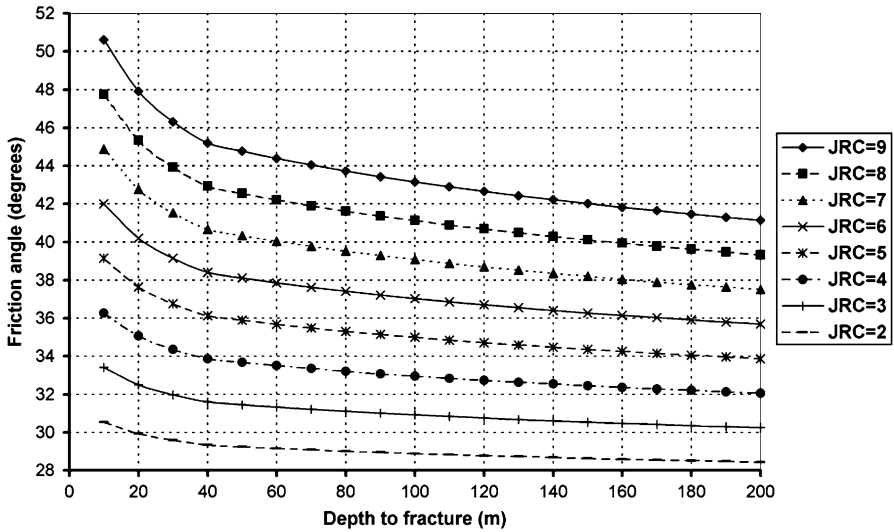
Fig. 15 Active friction angle versus depth at different JRC for a fracture with dip 35°. The depth to groundwater is 40 m

as the normal stress itself had much more effect on the results than any other input parameter. The computed values for a fracture with dip 35° are shown in Figs. 16 and 17.
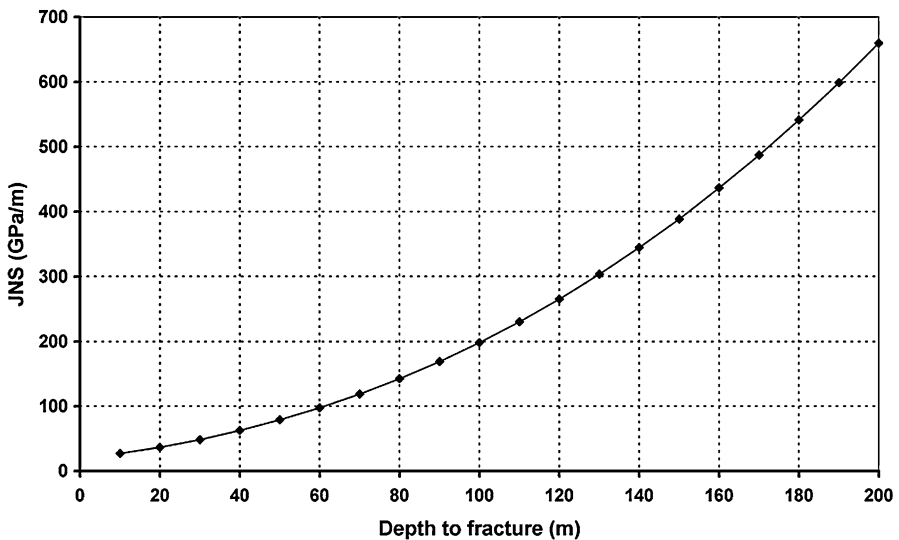
Fig. 16 Joint normal stiffness versus depth for a fracture with dip 35°

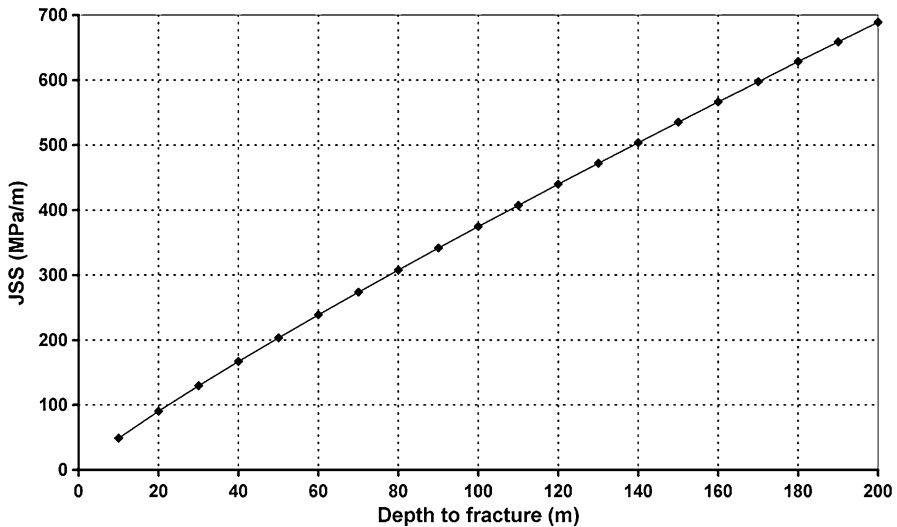**Fig. 17** Joint shear stiffness versus depth for a fracture with dip 35°

3.6 Groundwater

The depths to groundwater were measured at about 53 m in the upper borehole between August 2005 and January 2006, at about 40 m in the middle borehole for August 2005–September 2006 and at about 40 m in the lower borehole for August 2005 to October 2006. Several springs exist at the site, most being observed in the area below (south of) the Toe Zone, mainly at an elevation of about 100 m.a.s.l. (between the Toe Zone and the fjord, Fig. 2). Groundwater at shallow depth in the lower part of the slope, towards the fjord, is also indicated by shallow penetration depth of the ground-penetrating radar (Ganerød et al. 2008). In models where the groundwater table was assumed constant, it was defined at 50 m below the surface from the position of the upper borehole and up-slope and rose linearly to 40 m below the surface between the upper borehole and the middle borehole. The groundwater table was defined at 40 m below the surface between the middle and the lower borehole and rose linearly further down-slope to the ground surface at an elevation of 100 m.a.s.l. (Fig. 34).

Displacement measurements from the three extensometers located across the upper extension fracture started in August 1993 and do not in general show any strong seasonal effect (Kveldsvik et al. 2006). The displacements were related to varying groundwater level during Spring 2006 as indicated by the groundwater monitoring in the middle borehole, laser measurements in the northwestern flank and the rod extensometers (locations are shown in Fig. 6). The groundwater level increased 4 m over 2 weeks before it decreased quickly back to normal by 5 May 2006. From 6 May the distance between the two lasers and their respective reflectors increased anomalously during a period of about 2 weeks before the displacement rate became normal again. Starting from 3 May decreased distances across the upper

crack of up to 2 mm were measured by the extensometers over a few days before
they increased quickly again. The short duration in distances across the upper crack
indicates block rotation.

4 Division of the Unstable Area into Blocks

4.1 Initial Block Model

The initial block division layout in Figs. 6, 7 and 8 is hereafter referred to as block
model 1. The block numbering of block model 1 was used throughout the text
although the block boundaries were changed, meaning that the shape and area of,
say block 5, in block model n could be different from block 5 in block model 1. If a
single block from block model 1 was split into two blocks, e.g. block 5 was split into
a western and an eastern part, the two new blocks were subsequently named blocks
5W and 5E.

4.2 Block Models Derived from the 2004 to 2006 Displacements

The result of block model 1 is shown in Fig. 18. The measured displacements rates
were multiplied by 500 in this model, as in subsequent models, for better
visualization of the results. The average displacement error for this model was 0.18
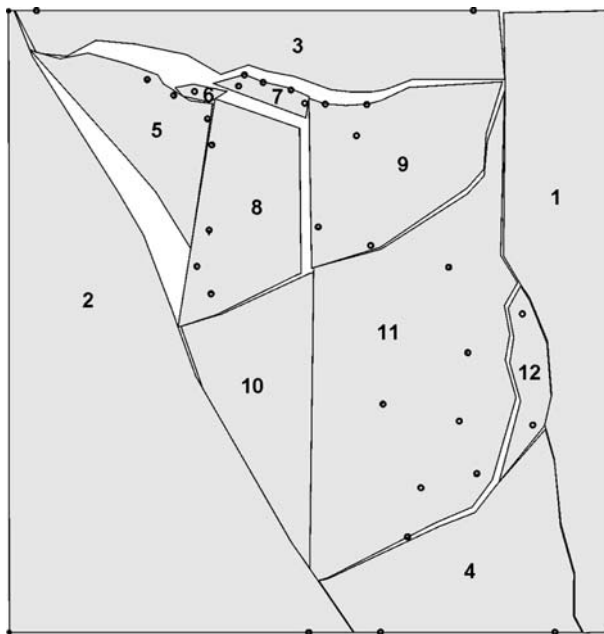
Fig. 18 Block model 1 after computation by DDA-Backward; 2004–2006 displacements/year are scaled
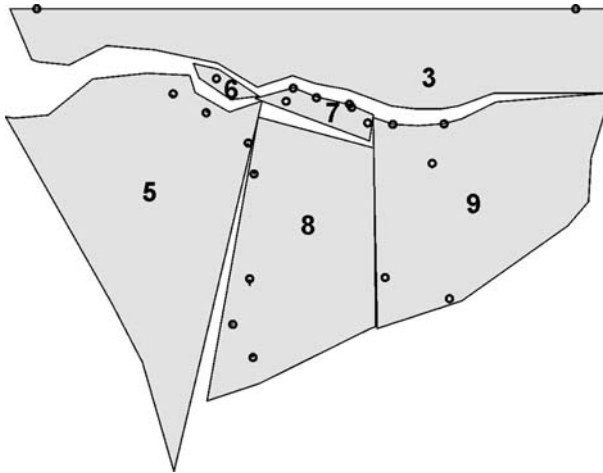up by 500. Average displacement error = 0.18

(18%), but by comparing Fig. 18 with Fig. 6 it is seen that large block deformations occurred in the model, especially in block 5, i.e. it is not an acceptable model. Since the eastern lower part does not show much movement in any of the data sets, and data do not exist for the western lower part, these blocks (10, 11 and 12) and three of the blocks outside the boundaries of the assumed unstable area (1, 2 and 4) were removed to investigate possible refinements of the block model in the upper part. By removing these blocks it is presupposed that the upper blocks have to move independently of the lower blocks.

Block 6 is a graben that consists of loose blocks, and it has moved approximately in a SE direction from 2004 to 2006. It is seen as a block with displacement error equal to zero and large deformation in Fig. 18. The photogrammetry (Figs. 7, 8) shows even more easterly movement. Block 6 is most reasonably defined as a separate block in a model, but it does not fit a model with contact between the block boundaries. The measured displacements in block 6 may represent internal movements near the surface and the directions of the movements measured in the graben are subparallel to the dip direction of the terrain in the graben (Fig. 19). As illustrated in Fig. 19 a gap between the blocks (block 6 and block 5) also exists today, and also existed in 1961, i.e. the zero point of the measured displacements. It appears that the measured movements in the graben (block 6) can be explained by the local topography as the terrain surface in the graben dips in an approximately in a SE direction whereas the surrounding terrain dips in a S–SW direction. The measured displacement of block 6 was removed in all models presented hereafter since it was considered unnecessary to include this displacement to evaluate the models.

Block model 2, which consisted of the upper blocks (3, 5, 6, 7, 8 and 9), is shown in Fig. 20. The average displacement error of block model 2 was 0.14 and large strains were visible in block 5 (compare Fig. 20 with Fig. 6); large strains are also shown in Fig. 25. The average displacement error of block models 3, 4A, 4B and 5 (Figs. 21, 22, 23 and 24) was 0.10. The strains were also about equal in these block

Fig. 19 Graben (block 6 in Fig. 6) looking towards ESE. The difference in the measured surface movement directions is indicated by *arrows*

Fig. 20 Block model 2 after computation by DDA-Backward; 2004–2006 displacements/year are scaled up by 500. Average displacement error = 0.14
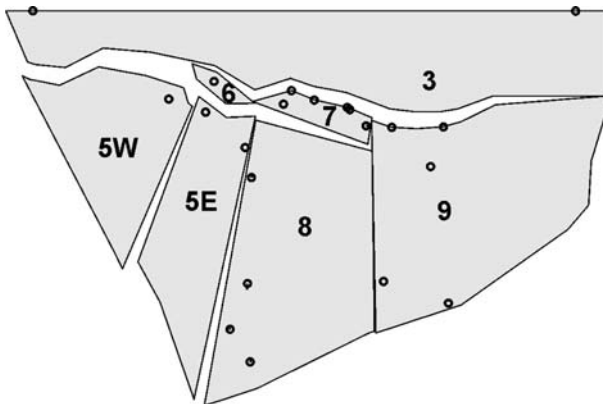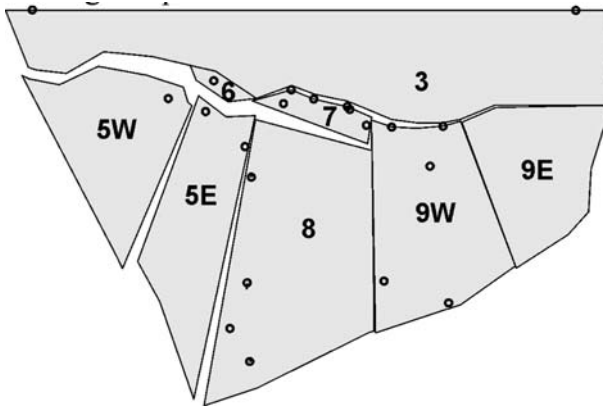

Fig. 21 Block model 3 after computation by DDA-Backward; 2004–2006 displacements/year are scaled up by 500. Average displacement error = 0.10

models, except in block 3. An example of equal strains is shown in Fig. 26. Block 3 was deformed in block model 3, which did not happen in block model 4 and 5. This is seen in Figs. 21, 22, 23 and 24 by the larger upper gap in Fig. 21 compared with Figs. 22, 23 and 24. The larger gap occurred because block 3 was pushed upwards in block model 3 (and block model 2). Upward push did not occur in block models 4 and 5 where block 9 was split into two parts, blocks 9W and 9E. This is also illustrated in Fig. 27.

The only difference between block models 4A and 4B was that block 9E was fixed (measuring point with displacement equal to zero) just east of the boundary between block 9W and 9E and just south of the Back Scarp Zone, more exactly at
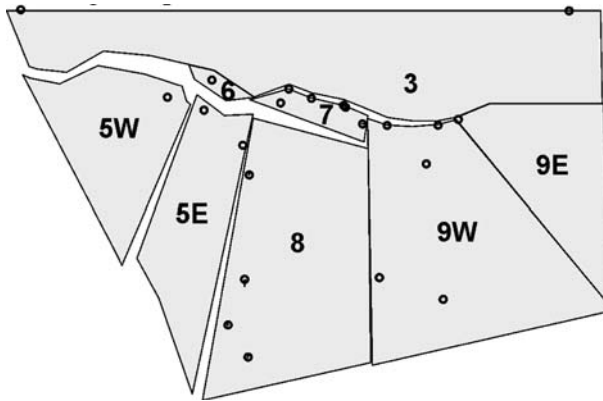
Fig. 22 Block model 4A after computation by DDA-Backward; 2004–2006 displacements/year are scaled up by 500. Average displacement error = 0.10
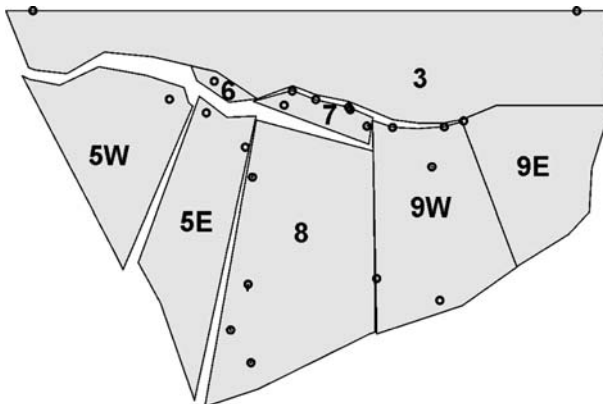

Fig. 23 Block model 4B after computation by DDA-Backward; 2004–2006 displacements/year are scaled up by 500. Average displacement error = 0.10

the location where the upper tension crack is no longer visible as an open crack. This is seen in Fig. 23 where there is no gap between block 9E and block 3. Block models 4A, 4B and 5 were ranked equally based on the computations. Merging block 10 with block 8, i.e. assuming that block 10 without measuring points moves together with block 8, gave the same results.

Different models of the lower eastern part were tested, i.e. the area with blocks 11 and 12 (Fig. 18). Splitting block 11 into a western part and an eastern part was tested as well as different boundaries between the northern part and the southern part, i.e. varying the boundary between block 9 and block 11. The best fit model, block model 6, is shown in Fig. 28. The average displacement error was equal to zero. The northern boundary of block model 6 corresponds to the southern boundary of block model 5 (Fig. 24). Thus one can conclude that the best fit model is block model 5 combined with block model 6. Further, block 10, which is adjacent to the

Fig. 24 Block model 5 after computation by DDA-Backward; 2004–2006 displacements/year are scaled up by 500. Average displacement error = 0.10
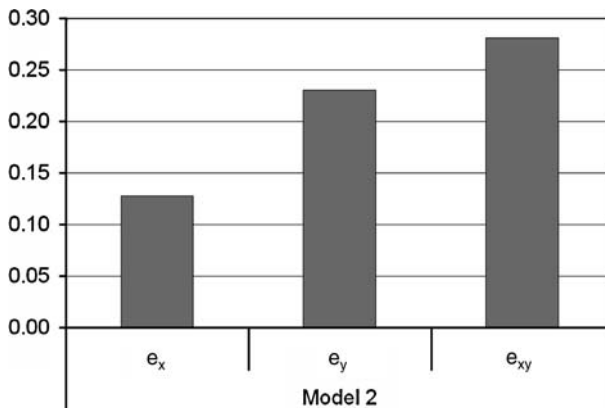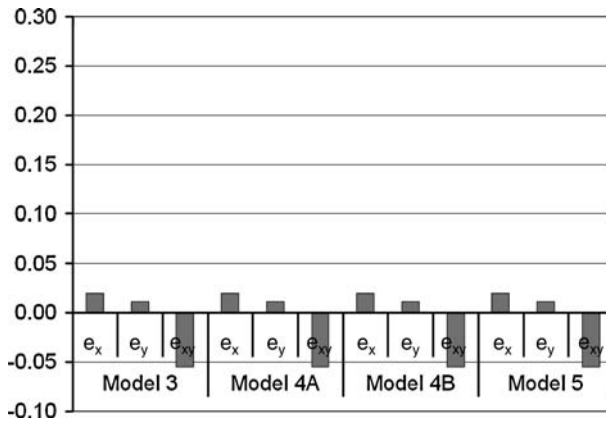

Fig. 25 Strains in block 5. Block model 2. e_x strain along the x-axis (EW), e_y strain along the y-axis (NS), e_{xy} total shear strain

Western Boundary Zone (Figs. 2, 6), may or may not move together with block 8. Block 11 does not move.

4.3 Block Models Derived from the 1961 to 1983 Displacements

The measured displacements in the lower part (in block 11 with the exception of the three northernmost points) were not sufficient to draw block boundaries (Fig. 7). They indicate that the majority of block 11 did not move much between 1961 and 1983. DDA-Backward computations were therefore performed only on the northern part. The three northernmost measuring points in block 11 were included in block 9, i.e. the boundary between block 9 and block 11 as shown in Fig. 7 was moved southwards in Fig. 29. The eastern measuring point in block 9 with displacement towards SE does not seem very reliable compared with the neighbouring points,

Fig. 26 Strains in block 5E. Block models 3–5. e_x strain along the x-axis (EW), e_y strain along the y-axis (NS), e_{xy} total shear strain
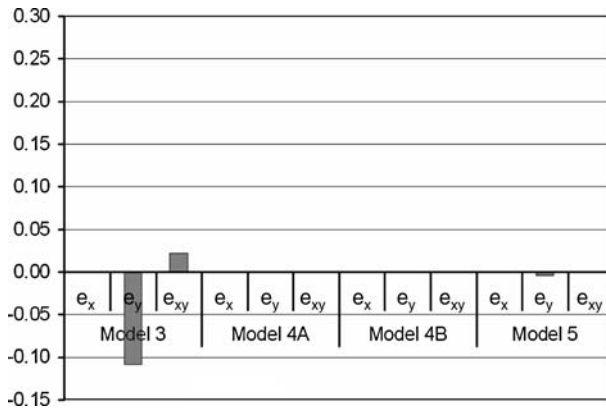

Fig. 27 Strains in block 3. Block models 3–5. e_x strain along the x-axis (EW), e_y strain along the y-axis (NS), e_{xy} total shear strain

including the 1983–2004 displacements (Fig. 8). The eastern measuring point of block 9 was therefore removed from the data set. The two measuring points in block 6 were also removed for reasons explained previously.

The models that were ranked highest and about equal with respect to the average displacement error (0.20–0.22) and strains are shown in Figs. 29, 30 and 31. Block model 7 (Fig. 29) resulted in the best fit with respect to the closure of the upper crack and may therefore be regarded as better than block models 8 and 9 (Figs. 30, 31). It should be noted that the westernmost block, block 5, which was equal in all models, was measured only at one point (Fig. 7). This measurement strongly indicates that an area of the northernmost western flank moved in a near-SW direction, however the size and shape of this area/block is very uncertain as it is based on just one measuring point.

Fig. 28 Block model 6 after computation by DDA-Backward; 2004–2006 displacements/year are scaled up by 500. Average displacement error = 0.0
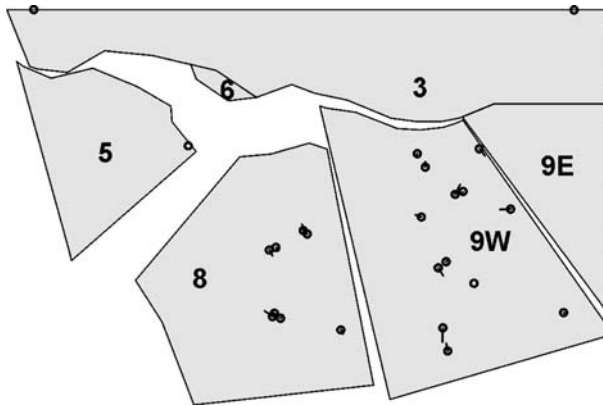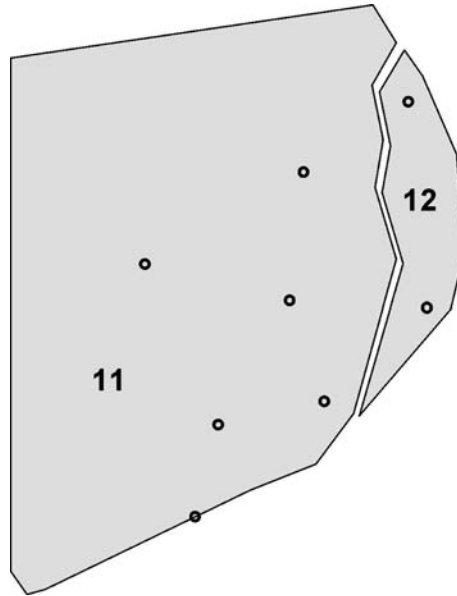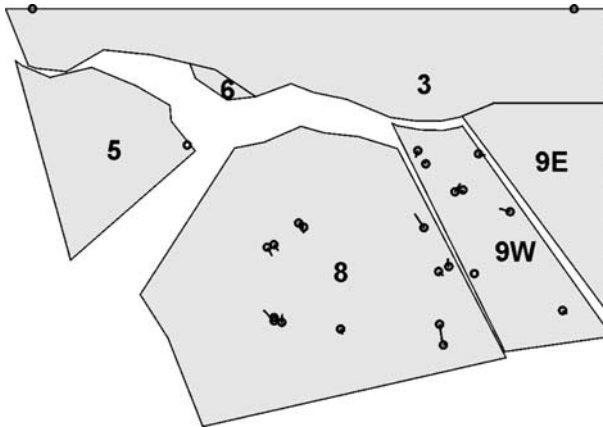

Fig. 29 Block model 7 after computation by DDA-Backward; 1961–1983 displacements/year are scaled up by 500. Average displacement error = 0.21

4.4 Block Models Derived from the 1983 to 2004 Displacements

This data set was used only for the purpose of finding the best fit boundary between the western and the eastern upper part of the slope.

The two measuring points in and near block 6, the graben (Fig. 8), were again removed from the data set for the same reasons as described in Sect. 4.2 as were all measuring points in block 9. The latter was based on the scatter of displacement directions (Fig. 8) and as all the measuring points indicate that this part of the slope

Fig. 30 Block model 8 after computation by DDA-Backward; 1961–1983 displacements/year are scaled up by 500. Average displacement error = 0.22

Fig. 31 Block model 9 after computation by DDA-Backward; 1961–1983 displacements/year are scaled up by 500. Average displacement error = 0.20
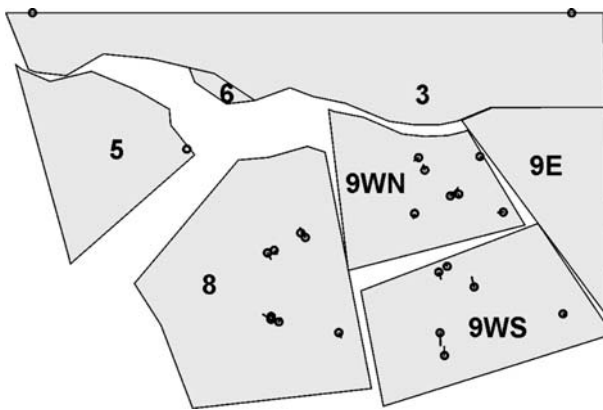
did not move appreciably from 1983 to 2004. Figure 32 shows block model 10 (excluding the data points described above) after computation. Deformation of block 8 occurred, and this is seen by the fact that block 9 was pushed out of position. The average displacement error was 0.28, and the lack of trend in the errors suggests that an obviously better model does not exist.

4.5 Conclusion and Discussion of DDA Model Results

The overall conclusion based on all three data sets is that the upper part of the slope can be divided into four or five relatively large blocks by block boundaries in an approximately N–S-direction of which block 9E does not move (Fig. 33). The
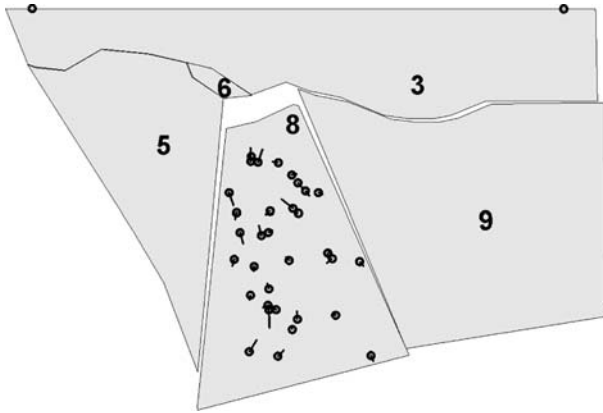
Fig. 32 Block model 10 after computation by DDA-Backward; 1983–2004 displacements/year are scaled up by 500. Average displacement error = 0.28
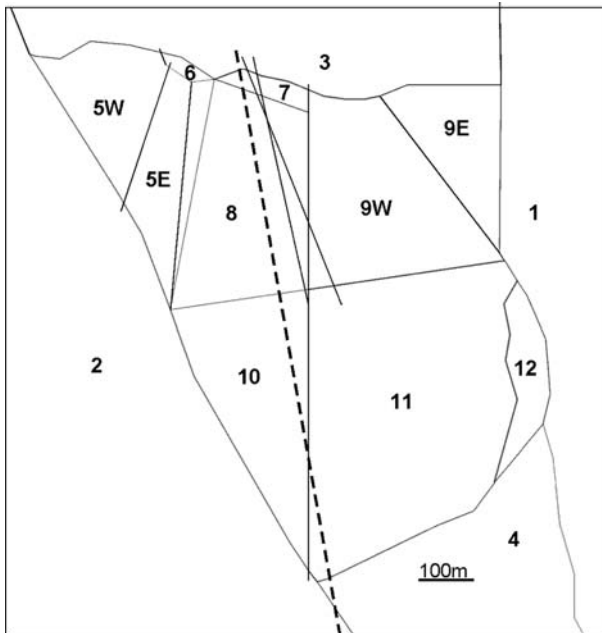

Fig. 33 Possible block boundaries. The *black broken line* shows the location of the profile that was used for the numerical modelling of vertical cross sections

western part that moves in a SSW–SW direction may consist of one (block 5) or two blocks (block 5W and block 5E), and limited data here make both options possible. It should be noted that the slope is very steep near the measured displacement(s) in the direction of the Western Boundary Zone (Fig. 2). It is therefore highly possible that the block(s) represented by the measured displacements (Fig. 6, 7) is/are small

in the upper western part. The sliding surface may thus daylight in the steep terrain less than 100 m SSW of the Back Scarp Zone. If this is the case the remaining part of block 5 may or may not take part in a deeper block movement. Radar measurements from a position across the fjord were conducted for one period in 2005 and two periods in 2006. A large portion of the block below (SSW of) the steepest part of block 5 was also moving according to radar measurements, indicating that block 5 may be as large as shown in Fig. 33.

The central part of the upper slope (blocks 8 and 9W in Fig. 33) must be divided into two blocks in approximate N–S direction based on the 1961–1983 (Fig. 7) and 2004–2006 (Fig. 6) data sets. The 1983–2004 data set includes most data in block 8 and probably defines block 8 better than the other data sets (Figs. 8, 32). The boundary between block 9W and the stationary block 9E appears to be orientated about NW–SE to NNW–SSE.

Two small blocks (6 and 7) have been identified by the 2004–2006 data set (Figs. 6, 20, 21, 22, 23 24 and 33). The displacement measured in block 6 may represent only near-surface movements. Block 7 clearly shows less movement than block 8. It should be noted that the magnitude of the displacements measured in the period 2004–2006 across and near the Back Scarp Zone are smaller or similar to the magnitude of the accuracy of the photogrammetric method (0.5 m in 21–22 years), which may explain at least partly why block 7 is not indicated in these data sets (Figs. 7, 8, 29, 30, 31 and 32). The block boundary between the upper and the lower halves of the slope seems to be located slightly more to the south than shown in Figs. 2 and 6.

A considerable portion of the lower half of the slope moves little or not at all according to the 2004–2006 displacement data. The limited amount of displacement data raises questions on the western part defined by block 10 with the boundary towards block 11 possibly being located more to the east than shown in Fig. 33. The fact that rock slides have occurred on the western flank of block 10 in 1940 and about 1960 (Kveldsvik et al. 2006) may indicate that movements take place in this part of the slope.

The uncertainties in a DDA-Backward analysis increase with decreasing amount of displacement data. This study made it clear that the amount of data for the whole slope is rather limited for DDA-Backward computations to be performed. However, when used in combination with the geological model proposed by Ganerød et al. (2008), possible/plausible block boundaries have been identified. When related to the geological model, the study presented herein showed that the boundary between the upper (northern) part that moves and lower (southern) part that does not move may be traced in a more west-east orientation than proposed by Ganerød et al. (2008) (compare Fig. 33 with Figs. 2 and 6). Furthermore, the upper part may be subdivided into more blocks than proposed by Ganerød et al. (2008), who also suggested dividing the lower part into two subdomains based only on geophysical data (subdomains III and IV in Fig. 3). The displacement data were too limited in the lower part to test this hypothesis. For the same reason the location of the Toe Zone could not be analysed by the DDA-Backward method.

5 Stability Analysis of Vertical Cross Sections

5.1 Model Description

The actual location of the analysis profile is shown in Figs. 2 and 33. As the slope geometry does not vary significantly the profile is fairly representative for the western and central part with a direction of approximately N150°–N180°.

The fracture geometry (block model) is shown in Fig. 34. The positions at the model surface of the upper and lower outcropping fractures correspond with the boundary between the upper and lower part and the Toe Zone of the DDA-Backward model (Fig. 33). The friction angles derived from the JRC and the estimated effective normal stress (Eq. 5, Fig. 15) were assumed constant at depths of 10, 20 m, etc. for each of the foliation fractures with an inclination of either 35° or 32°. The depth to the outcropping fractures varies along the fractures and they were divided into 100-m-long segments having different friction angles. The
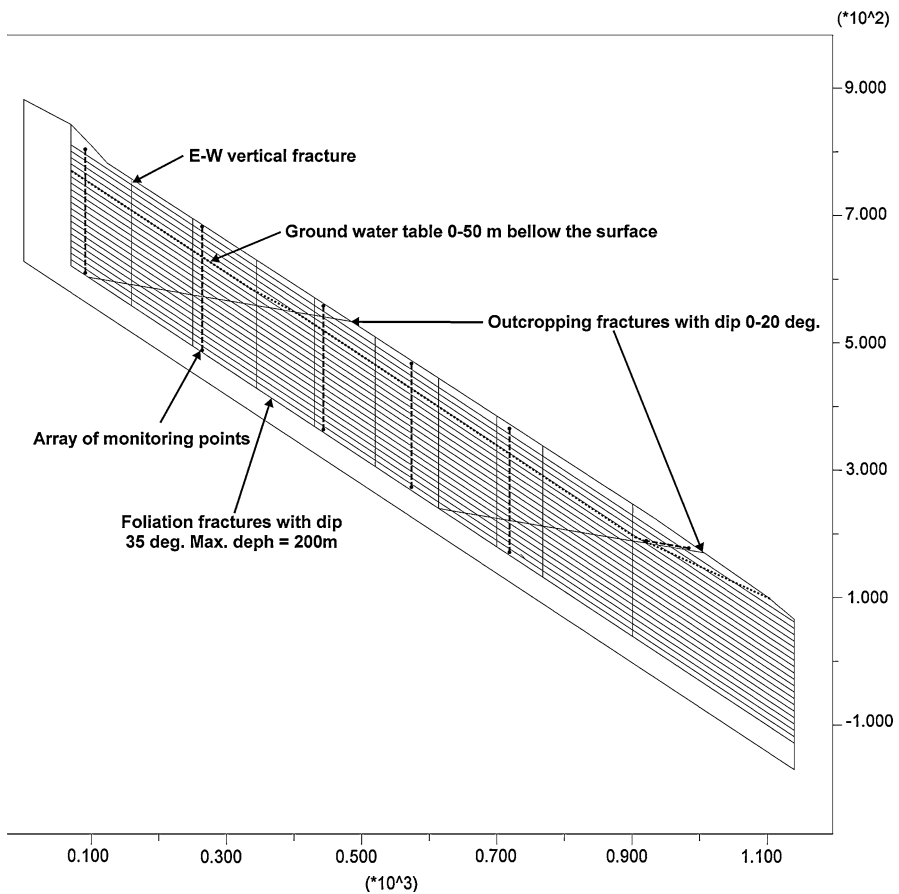
Fig. 34 Block model

average depth to the fracture over each 100-m-long segment was used for estimating the effective normal stress (Eq. 3) and the corresponding friction angle. For comparison, some models with constant friction angles for all foliation fractures and outcropping fractures were also computed. A maximum depth of the instability less than 200 m was obtained by gluing varying lengths of the inner part of the outcropping fractures using assumed high shear resistance properties.

The left-hand side, right-hand side and the base of the model were fixed and gravity was applied before computation. The mesh geometry was designed with an aspect ratio of approximately 0.4 in the fractured area of the model.

5.2 Results

The results of the numerical modelling using UDEC are shown in Table 1.

Models with E–W fractures spaced 45 m (instead of 90 m) and models with friction angle of E–W fractures equal to 35° (instead of 49.5°) were also computed. The differences in behaviour due to these changes were moderate and of no practical influence on the conclusions drawn from the computations reported in Table 1.

Upward displacements may take place in the slope (see Sect. 3.2.1). A hypothetical geometry that would result in considerable upward displacements is demonstrated in Fig. 37. The fixed part of the lower outcropping fracture could be due to obstacles (folding) and/or rock bridges between fractures.

5.3 Conclusions and Discussions of UDEC Modelling Results

5.4 The Following Observations and Discussion can be made:

1. The models that were unstable to the greatest depth agreed better with the shear strength parameters collected for the unstable area and the computations performed for a rock slide that occurred in about 1960 than the models that were unstable to shallower depths. As described previously the average JRC of the foliation fractures was 7.8, the safety factor for the rock slide that occurred in about 1960 equalled unity for JRC equal to 6.0 and the inclination of the failure surface of the rock slide was about 41° (Kveldsvik et al. 2007).
2. The depth of the instability was governed by the depth of the lower outcropping fracture (the lower fold daylighting in the Toe Zone with reference to Fig. 3) for models with groundwater (see the example in Fig. 35).
3. The limiting JRC increased with increasing depth of the potential instability, i.e. stability decreased with depth.
4. The limiting JRC increased with increasing inclination of the outcropping fracture.
5. The upper outcropping fracture acted as a sliding plane (for a shallow instability, see the example in Fig. 36) only when sliding was prevented on the lower outcropping fracture (which could be due to obstacles and/or rock bridges), and the limiting JRC for the upper part of the slope was much lower

Table 1 Results from computations using UDEC

Model[a]	Groundwater table	Limiting friction[b]: JRC or φ (°)	Unstable at[b]: JRC or φ (°)	Max. depth of instability (m)
Model-200-35-0-2	As shown in Fig. 34	6	5	200
Model-200-35-10-2	As shown in Fig. 34	7	6	200
Model-200-35-20-2	As shown in Fig. 34	8	7	190
Model-200-32-20-1-only lower outcropping fracture[c]	As shown in Fig. 34	8	7	200
Model-110-35-20-2	As shown in Fig. 34	7	6	110
Model-70-35-20-2	As shown in Fig. 34	6	5	70
Model-30-35-20-2	As shown in Fig. 34	4	3	30
Model-130-35-20-1-only upper outcropping fracture	As shown in Fig. 34	4	3	20
Model-200-35-20-2-constant friction angles	As shown in Fig. 34	40	39	180–190
Model-200-35-20-2-30 m removed[d]	As shown in Fig. 34	10	9	190
Model-200-35-20-2-GW10[e]	As shown in Fig. 34 first, then rose by 10 m	8	Stable after raising the GW table by 10 m	
Model-200-35-20-2-GW20[e]	As shown in Fig. 34 first, then rose by 20 m	8	Unstable to 190 m after elevating the GW table by 20 m	
Model-70-35-20-2-GW10[e]	As shown in Fig. 34 first, then rose by 10 m	6	Unstable to 70 m after elevating the GW table by 10 m	
Model-200-35-10-2-dry	No water	4	3	90
Model-200-35-10-2- dry	No water	34	33	30

[a] Model-maximum depth of instability-inclination of foliation fractures-inclination of outcropping fractures-number of outcropping fractures-other info

[b] "Limiting friction": friction angles which were just large enough to result in equilibrium in a model. "Unstable at": friction angles which resulted in a "modest" unstable model. See also Sect. 2.2

[c] Foliation fractures having dip slightly less than the slope surface

[d] The whole model was computed to equilibrium first, and then all blocks down to the depth of 30 m were deleted to simulate a shallow slide above the groundwater table and computation was resumed

[e] Computation of models that were stable with the groundwater table as shown in Fig. 34 was resumed after the groundwater table was rose by 10 or 20 m. The limiting JRC for these models refers to the state of the model before the groundwater table was elevated.

than for the whole slope when deep sliding on the lower outcropping fracture was possible. This indicates that a shallow instability only in the upper part caused by an upper outcropping fracture is not very likely.

6. The limiting JRC increased from 8 to 10 when a 30-m-deep slide took place in the model and the groundwater table was constant. This shows that a possible rock slide suggested by the movements at this depth (Sect. 3.2.2) may reduce the stability at greater depth.
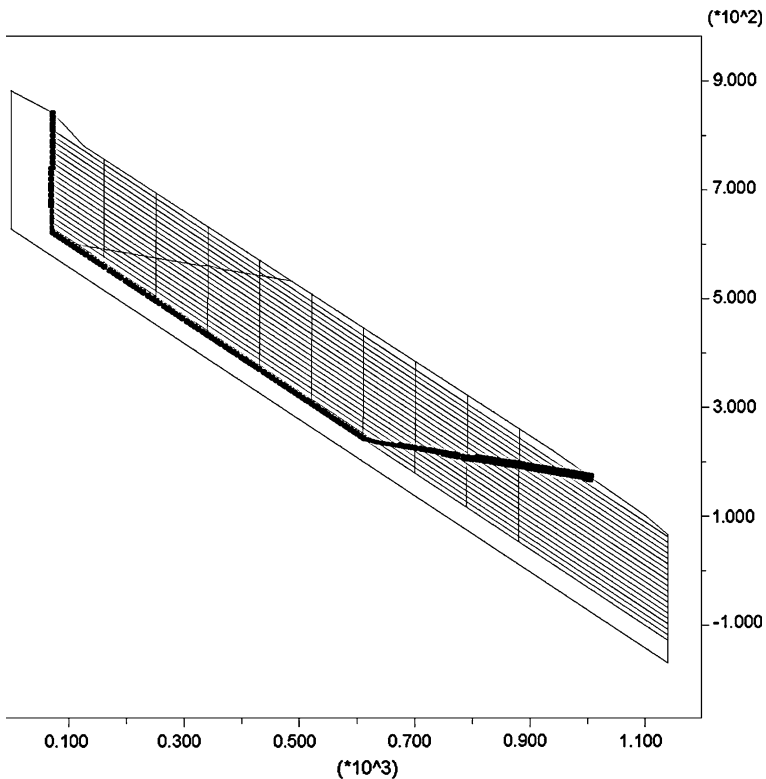
Fig. 35 Maximum magnitude of simulated shear displacements at a depth of 200 m and at the lower outcropping fracture

7. Model-200-35-20-2 retrieved stability after a period of increased movements when the groundwater table was elevated by 10 m from the groundwater table shown in Fig. 34, but model 70-35-20-2 did not. This indicates that increased water pressure is less critical for a possible very deep slope instability than a less deep instability.

8. Model-200-35-10-2-dry was unstable to half the depth of its corresponding model with groundwater, requiring much smaller JRC. This illustrates the very adverse effect that may be caused by the presence of groundwater regarding possible slide volumes.

9. Constant friction instead of stress-dependent friction did not change the depth of the instability for the models with groundwater, but it reduced the depth of instability considerably for the dry models.

10. Most of the shear displacements took place at the base of the unstable rock mass and at foliation fractures nearest to this base in all the models that were unstable below the groundwater table. Shear displacements of about the same magnitude took place at 10, 20 and 30 m, respectively, in the two models that were unstable to a 30 m depth. In the dry model that was unstable to 90 m

(*10^2)

9.000

7.000

5.000

3.000

1.000

-1.000

0.100   0.300   0.500   0.700   0.900   1.100
(*10^3)
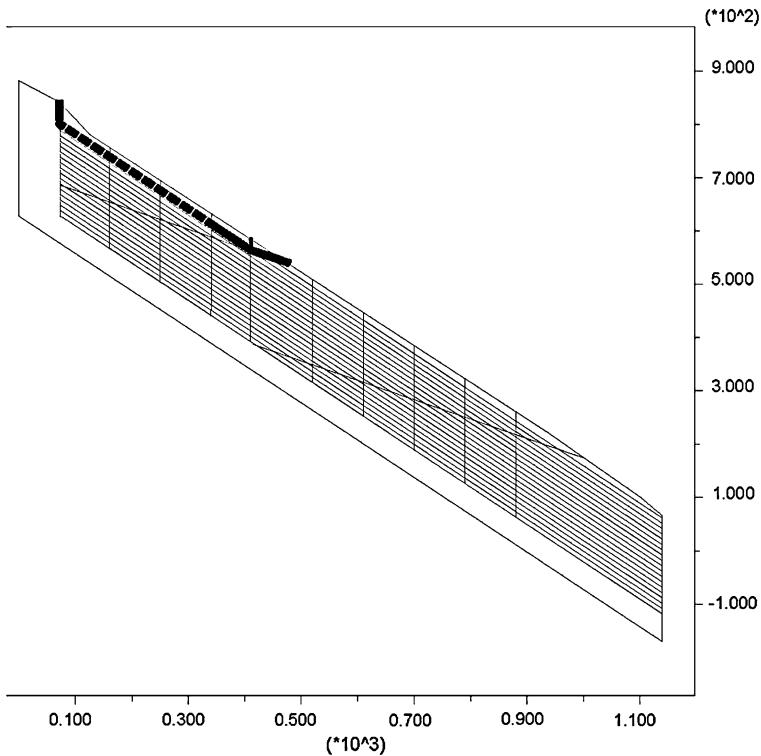
Fig. 36 Maximum magnitude of simulated shear displacements at a depth of 20 m and at the upper outcropping fracture

depth, the shear displacements from 10 to 30 m depth were of about the same magnitude and considerably larger than the shear displacements at greater depth, which were smallest between 70 and 90 m depth. This shows that possible large displacements at shallow depth (not measured yet) might be taken as an indication that the entire slope is actually unstable only to a shallow depth.

6 Overall Conclusions and Concluding Remarks

The upper part of the Åknes rock slope can divided into four or five blocks with block boundaries in the approximate N–S-direction of which the eastern block is stationary, i.e. three or four blocks may be considered as potential areas that may fail catastrophically. A considerable portion of the lower half of the slope is moving negligibly according to the 2004–2006 displacement data. The limited amount of displacement data in the lower part raises questions about the southwestern part of
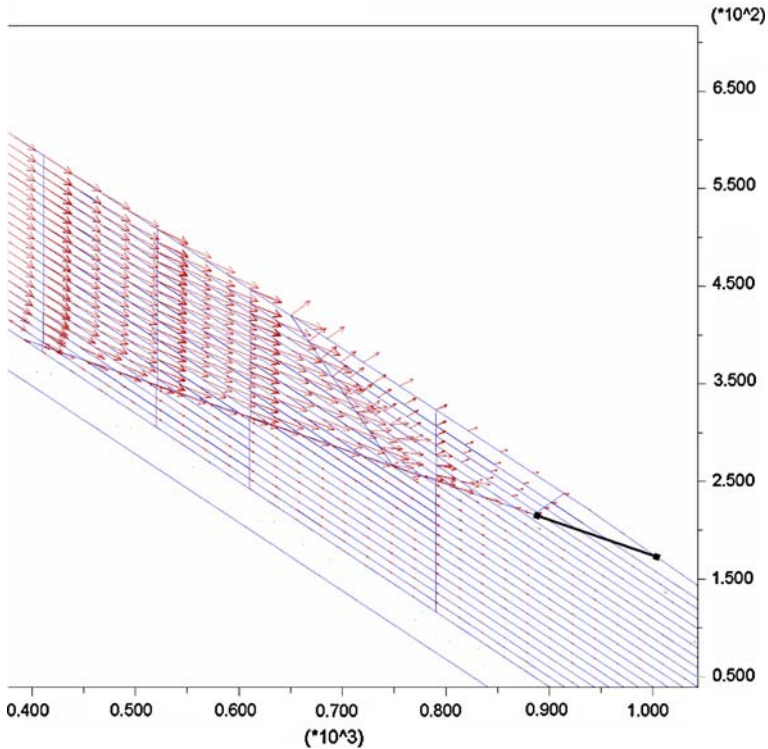
Fig. 37 Hypothetical geometry that resulted in upward displacement in the lower part of the slope. The *thick black line* marks the fixed part of the lower outcropping fracture

the slope. As the southwestern part is located down-slope of the upper part that is documented to be moving at the highest rate (Fig. 6, 7, 8), future measurements in this area should be implemented in the early warning system. Whether the southwestern part does not move, moves slower, or perhaps more discontinuously, than the areas just up-slope may make a difference in the possible development towards a potential catastrophic failure. Stresses may build up in the southwestern part and the early signs of a development towards a catastrophic failure, i.e. accelerated movements, may be picked up sooner here than up-slope in that movements may accelerate slightly earlier than up-slope or the lower part may start moving from a previous apparent stationary state.

The Åknes rock slope may be unstable to great depth. Constraining the depth is a key issue with respect to estimating the worst-case volumes that may fail catastrophically, and consequently the worst-case magnitude of the resulting tsunami. Probably the best method to constrain the depth of the instability is to measure displacements in the boreholes at other depths than has been done to date. Measuring water pressure at different depths in the boreholes should also be carried out as the groundwater conditions may play an important role in defining sliding surfaces deeper than about 40 m.

References

Barton N, Bandis S (1990) Review of predictive capabilities of JRC-JCS model in engineering practice. In: Proc Int. Symp. on Rock Joints, Loen, Norway, Balkema, pp. 603–610

Barton N, Choubey V (1977) The shear strength of rock joints in theory and practice. Rock Mech 10:1–54

Bhasin R, Kaynia AM (2004) Static and dynamic simulation of a 700 m high rock slope in western Norway. Eng Geol 71:213–226

Blikra LH, Longva O, Harbitz C, Løvholt F (2005) Quantification of rock-avalanche and tsunami hazard in Storfjorden, western Norway. In: Senneset K, Flaate K, Larsen JO (eds) Landslide and Avalanches ICFL 2005 Norway. Taylor & Francis, London, pp 57–63

Blikra LH, Longva O, Braathen A, Anda E, Dehls JF, Stalsberg K (2006) Rock-slope failures in Norwegian fjord areas: examples, spatial distribution and temporal patterns. In: Evans SG, Mugnozza GS, Strom A, Hermanns RL (eds) Landslides from Massive Rock Slope Failure. NATO Science Series. IV. Earth and Environmental Sciences, vol 49, pp 475–496. Springer, Dordrecht

Blikra LH (2008) The Åknes rockslide; monitoring, threshold values and early-warning. In: Proceedings of the 10th International Symposium on Landslides and Engineered Slopes, Xi'an, China (In print)

Braathen A, Blikra LH, Berg SS, Karlsen F (2004) Rock-slope failures of Norway; type, geometry, deformation mechanisms and stability. Norwegian J Geol (NGT) 84:67–88

Chang QT (1994) Nonlinear dynamic discontinuous deformation analysis with finite element meshed block systems. Ph.D. thesis, University of California, Berkeley

Crosta GB, Agliardi F (2003) Failure forecast for large rock slides by surface displacement measurements. Can Geotech J 40:176–191

Cundall PA (1980) UDEC—a generalized distinct element program for modelling jointed rock. Report PCAR-1-80, Peter Cundall Associates, European Research Office, US Army Corps of Engineers

Derron M-H, Blikra LH, Jaboyedoff M (2005) High resolution digital elevation model analysis for landslide hazard assessment (Åkerneset, Norway). In: Senneset, Flaate K, Larsen JO (eds) Landslide and Avalanches ICFL 2005 Norway. Taylor & Francis Group, London, pp 101–106

Eiken T (2007) Personal communication. University of Oslo, Norway

Eberhardt E, Stead D, Coggan JS (2004a) Numerical analysis of initiation and progressive failure in natural rock slopes—the 1991 Randa rockslide. Int J Rock Mech Mining Sci 41(1):69–87

Eberhardt E, Spillmann T, Maurer H, Willenberg H, Loew S, Stead D (2004b) The Randa Rockslide Laboratory: establishing brittle and ductile instability mechanisms using numerical modelling and microseismicity. In: Lacerda A et al. (eds) Proc. 9th Int. Symp. on Landslides. Rio de Janeiro. Balkema, Leiden, pp 481–487

Evans SG, Mugnozza GS, Strom AL, Hermanns RL, Ischuk A, Vinnichenko S (2006) Landslides from massive rock slope failure and associated phenomena. In: Evans SG, Mugnozza GS, Strom A, Hermanns RL (eds) Landslides from Massive Rock Slope Failure. NATO Science Series. IV. Earth and Environmental Sciences, vol 49. Springer, Dordrecht, pp 3–52

Fritz HM, Hager WH, Minor H-E (2001) Lituya Bay case: rockslide impact and wave run-up. Sci Tsunami Hazards 19(1):3–22

Fukuzono T (1985) A new method for predicting the failure time of a slope. In: Proceedings of the 4th International Conference and Field Workshop on Landslides, Tokyo, Tokyo University Press, pp 145–150

Ganerød GV, Grøneng G, Rønning JS, Dalsegg E, Elvebakk H, Tønnesen JF, Kveldsvik V, Eiken T, Blikra LH, Braathen A (2008) Geological model of the Åknes rock slide, western Norway. Eng Geol (in print)

Govi M, Gulla G, Nicoletti PG (2002) Val Pola rock avalanche of July 28, 1987, in Valtellina (Central Italian Alps). In: Evans SG, DeGraff JV (eds) Catastrophic landslides: effects, occurrence and mechanisms. Geol. Soc. Am. Rev. Eng. Geol., vol XV, pp 71–89

Hart RD (1993) An introduction to distinct element modelling for rock engineering. In: Hudson JA (ed) Comprehensive Rock Engineering: Principles, Practice and Projects, vol 2. Pergamon Press, Oxford, pp 245–261

Jing L (1998) Formulation of discontinuous deformation analysis (DDA)—an implicit discrete element model for block systems. Eng Geol 49:371–81

Jing L (2003) A review of techniques, advances and outstanding issues in numerical modelling for rock mechanics and rock engineering. Int J Rock Mech Mining Sci 40(7–8):283–353

Kilburn CRJ, Petley DN (2003) Forecasting giant, catastrophic slope collapse: lessons from Vajont, Northern Italy. Geomorphology 54:21–32

Kveldsvik V, Eiken T, Ganerød GV, Grøneng G, Ragvin N (2006) Evaluation of movement data and ground conditions for the Åknes rock slide. In: Proceedings of International Symposium on Stability of Rock Slopes in Open Pit Mine and Civil Engineering, pp 279–299. The South African Institute of Mining and Metallurgy (SAIMM)

Kveldsvik V, Einstein HH, Nadim F, Nilsen B (2007) Alternative approaches for analyses of a 100,000 m³ rock slide based on Barton–Bandis shear strength criterion. Landslides. http://ejournals.ebsco.com/direct.asp?ArticleID = 414B898789CF80825C7D. doi:10.1007/s10346-007-0096-x

MacLaughlin MM, Sitar N (1995) DDA for Windows: Discontinuous deformation analysis for the windows PC environment. Geotechnical engineering report no. UCB/GT/95-04, University of California, Berkeley, California

MacLaughlin MM, Berger EA (2003) A decade of DDA validation. In: Lu M (ed) Development and Application of Discontinuous Modelling for Rock Engineering. Proc. of the 6th International Conf. on Analysis of Discontinuous Deformation, Trondheim, Norway, pp 13–31. Balkema, Rotterdam, ISBN 90 5809 610 6

MacLaughlin MM, Doolin DM (2006) Review of validation of the discontinuous deformation analysis (DDA) method. Int J Numer Anal Methods Geomech 30(4):271–305

Müller-Salzburg L (1987) The Vajont catastrophe—a personal review. Eng Geol 24:493–512

Petley DN, Bulmer MH, Murphy W (2002) Patterns of movement in rotational and translational landslides. Geology 30(8):719–722

Segalini A, Giani GP (2004) Numerical model for the analysis of the evolution mechanics of the Grossgufer rock slide. Rock Mech Rock Eng 37(2):151–168

Shi GH, Goodman RE (1985) Two dimensional discontinuous deformation analysis. Int J Numer Anal Methods Geomech 9:541–556

Shi GH (1988) Discontinuous deformation analysis: a new numerical model for the statics and dynamics of block systems. Ph.D. Dissertation, Department of Civil Engineering, University of California, Berkeley

Shi G, Goodman RE (1989) Discontiuous deformation analysis—a new numerical method for the statics and dynamics of deformable block structures. In: Mustoe G et al. (eds) Proceedings of the 1st U.S. Conf. on Discrete Element Methods, Golden, Colorado. CSM Press, Golden, 16 pp

Shimizu N, Kakihara H, Terato H, Nakagawa K (1996) A back analysis for predicting deformational behaviour of discontinuous rock mass. In: Aubertin M, Hassani F, Mitri H (eds) Proceedings of the Second North American Rock Mechanics Symposium, Montreal, Canada, pp 2001–2008

Shyu K (1993) Nodal-based discontinuous deformation analysis. Ph.D. thesis, University of California, Berkeley

Sitar N, MacLaughlin MM, Doolin DM (2005) Influence of kinematics on landslide mobility and failure mode. J Geotech Geoenviron Eng 131(6):716–728

Stead D, Eberhardt E, Coggan JS (2006) Developments in the characterization of complex rock slope deformation and failure using numerical techniques. Eng Geol 83:217–235

Ter-Stepanian G (1966) Types of depth creep of slopes in rock masses. In: Proceedings of the first congress of the International Society of Rock Mechanics, Lisboa 1966, pp 157–160

Varga AA (2006) Gravitational creep of rock slopes as pre-collapse deformation and some problems in its modelling. In: Evans SG, Mugnozza GS, Strom A, Hermanns RL (eds) Landslides from Massive Rock Slope Failure. NATO Science Series. IV. Earth and Environmental Sciences, vol 49. Springer, Dordrecht, pp 103–110

Voight B (1989) A relation to describe rate-dependent material failure. Science 243:200–203

Yeung MR, Blair SC (1999) Analysis of large block test data using DDA method. In: Amadei B (ed) ICADD-3: Third International Conference on Analysis of Discontinuous Deformation. From Theory to Practice. American Rock Mechanics Association, Balkema, Rotterdam, Washington DC, pp 141–150

Yeung MR, Blair SC (2000) DDA back analysis of large block test data. In: Seattle WA, Girard J, Liebman M, Breeds C, Doe T (eds) Proceedings of Pacific Rocks, The Fourth North American Rock Mechanics Symposium. Balkema, Rotterdam, pp 934–944